Affinity-guided labeling reveals P2X7 nanoscale membrane redistribution during microglial activation.

Benoit Arnould,[1,†] Adeline Martz,[1,‡] Pauline Belzanne, [2,‡] Francisco Andrés Peralta[1,3] Federico Cevoli[1], Volodya Hovhannisyan[4], Yannick Goumon[4], Eric Hosy[2], Alexandre Specht[5], and Thomas Grutter[1,3,*].

[1]Laboratoire de Chémo-Biologie Synthétique et Thérapeutique (CBST) UMR 7199, équipe Ingénierie Canaux Ioniques, Centre National de la Recherche Scientifique, Université de Strasbourg, Faculté de Pharmacie, F-67400 Illkirch, France. [2]Interdisciplinary Institute for Neuroscience, CNRS, Université de Bordeaux, IINS, UMR 5297, Bordeaux, France. [3]University of Strasbourg Institute for Advanced Studies (USIAS), 67000 Strasbourg, France. [4]Centre National de la Recherche Scientifique-Unité Propre de Recherche (CNRS-UPR) 3212, Institut des Neurosciences Cellulaires et Intégratives, Unistra, Strasbourg, France. [5]Laboratoire de Chémo-Biologie Synthétique et Thérapeutique (CBST) UMR 7199, équipe NanoParticules Intelligentes, Centre National de la Recherche Scientifique, Université de Strasbourg, Faculté de Pharmacie, F-67400 Illkirch, France.

†Present address: Department of Chemistry, Washington University in St. Louis, St. Louis, Missouri 63130, USA.

‡These authors contribute equally.

*To whom correspondence should be addressed.

E-mail: grutter@unistra.fr).

Author Contributions: Conceptualization: TG; Data curation: PB, EH; Formal analysis: BA, AM, PB, FAP, EH, TG; Funding acquisition: TG; Investigation: BA, AM, PB, FAP, FC; Methodology: TG, BA, AM, PB; Project administration: TG; Resources: VH, YG; Supervision: TG, AS, EH; Visualization: TG; Writing—original draft: TG; Writing—review & editing: TG, BA, AS, EH.

Competing Interest Statement: Authors declare that they have no competing interests.

Keywords: purinergic receptors; inflammation; super-resolution microscopy; single-molecule.

This PDF file includes:

Main Text
Figures 1 to 6

Abstract

ATP-gated purinergic P2X7 receptors are crucial ion channels involved in inflammation. They sense abnormal ATP release during stress or injury and are considered promising clinical targets for therapeutic intervention. However, despite their predominant expression in immune cells such as microglia, there is limited information on P2X7 membrane expression and regulation during inflammation at the single-molecule level, necessitating new labeling approaches to visualize P2X7 in native cells. Here, we present **X7-uP**, an unbiased, affinity-guided P2X7 chemical labeling reagent that selectively biotinylates endogenous P2X7 in BV2 cells, a murine microglia model, allowing subsequent labeling with streptavidin-Alexa 647 tailored for super-resolution imaging. We uncovered a nanoscale microglial P2X7 redistribution mechanism where evenly spaced individual receptors in quiescent cells undergo upregulation and clustering in response to the pro-inflammatory agent lipopolysaccharide and ATP, leading to synergistic interleukin-1β release. Our method thus offers a new approach to revealing endogenous P2X7 expression at the single-molecule level.

Introduction

ATP serves as the primary energy carrier in cells and also functions as an extracellular signaling molecule. Normally, extracellular ATP levels are typically low in healthy interstitial fluid, but they rise at sites of stress or cellular injury, acting as a danger signal recognized as a damage-associated molecular pattern (DAMP). Extracellular ATP is detected by two families of purinergic receptors, metabotropic P2Y receptors and ionotropic P2X receptors (P2X1 to P2X7), with P2X7 specifically sensing abnormal ATP release in the mid-micromolar to low millimolar range (1-3). P2X7 is a transmembrane, non-selective cation channel (Na^+, K^+, Ca^{2+}) predominantly expressed in immune cells, such as macrophages and microglia (the resident macrophages of the central nervous system), where it plays a crucial role in inflammation and immunity (4, 5). Upon ATP binding, P2X7 activation triggers K^+ efflux, promoting the assembly of the NLRP3 inflammasome and leading to the maturation and secretion of pro-inflammatory mediators, including interleukin-1β (IL-1β) (6-11). P2X7 activation can cause cell death and is linked to the pathogenesis of several major disorders, including inflammatory pain (12), autoimmune diseases (13), tumor progression (14, 15), psychiatric conditions (16), anxiety-like behavior (17), and neurodegenerative diseases (18, 19), making P2X7 a clinically relevant target.

At the cellular level, P2X7 is expressed at the plasma membrane and associates with lipid rafts, which are membrane microdomains known to play a key role in the onset of inflammation (20-25). However, it is unknown how P2X7 is strictly distributed on the plasma membrane of cells and how its spatial and functional features intertwine in inflammatory conditions. Given the crucial role of P2X7 in inflammation and the growing interest in developing P2X7-targeted therapeutics, new approaches are needed to visualize P2X7 expression in immune cells at the single molecule level.

Numerous studies have investigated P2X7 expression in microglia using various experimental approaches, including functional assays (6, 26-28), radiolabeled ligand binding (29), immunofluorescence staining (30, 31), electron microscopy (32), and genetic manipulations (33). Although these studies confirmed the dominant expression of P2X7 in microglia, they provided only low-resolution cell imaging of P2X7, primarily due to the limitations of conventional light microscopy, which imposes a resolution restricted by the diffraction of light. Consequently, the detailed organization of P2X7 below ~250 nm remains unknown. This is a vital point, as recent data suggest that the spatial organization of cell membrane receptors may be a common regulatory mechanism for cellular signal transduction (34). However, it remains unclear whether such membrane organization similarly affects P2X7 signaling pathways.

Super-resolution microscopy techniques overcome this diffraction limit, enabling the visualization of fluorescently labeled membrane receptors at nanometric resolution (35, 36). To the best of our

knowledge, only two studies have reported super-resolved images of P2X7 (37, 38). The first study found P2X7 in lipid microdomains of an osteoblastic cell line (38), but the use of polyclonal antibodies to stain P2X7 raised questions about their selectivity (39). The second study involved fusing P2X7 to the photo-convertible fluorescent Dendra2 protein to track its dynamic organization in hippocampal neurons (37). While this study provided valuable insights into the nanometer-scale distribution of P2X7, it had three experimental biases. First, heterologous overexpression of P2X7-Dendra2 might not reflect native expression levels. Second, the C-terminal fusion of Dendra2 to P2X7 after the "ballast", a region that is critically involved in inflammation (5), could affect P2X7's pathogenicity. Third, there is growing evidence suggesting that neurons do not (or scarcely) express P2X7 (33), questioning the physiological relevance of investigating P2X7 nanoscale organization in hippocampal neurons. Therefore, these issues prompted us to develop a new, genetic-free strategy able to decorate endogenous P2X7 in native cells with fluorophores suitable for super-resolution imaging.

Among existing methods for labeling endogenous proteins in living cells, the affinity-driven reaction strategy involving protein-ligand interaction is of particular interest (40). It relies on the formation of a covalent bond on the protein that is guided by the affinity of a ligand bearing a reactive moiety. The efficiency of the labeling reaction depends on the chemical function of the reactive species. The recently developed *N*-acyl-*N*-alkyl sulfonamide (NASA) chemistry offers a suitable platform that enables the covalent transfer, under native cell conditions, of functional ligands to nucleophilic amino acid residues (typically lysine residues) located in close proximity to the ligand-binding site (41) (Figure 1A). In addition, NASA electrophilicity can be finely tuned by introducing of an electron-withdrawing moiety to the *N*-alky group, such as cyanomethyl, so that kinetic labeling can be considerably enhanced and carried out within minutes under physiological conditions (41).

Here, we report **X7-uP**, a P2**X7-u**nbiased **P**urinergic labeling reagent that efficiently biotinylates native P2X7 lysine residues via a *N*-cyanomethyl NASA-based chemical reaction driven by the affinity of AZ10606120, a highly selective P2X7 allosteric ligand. Using streptavidin-Alexa Fluor® 647 (Strept-A 647), we reveal the nanoscale distribution of P2X7 in BV2 cells at the single molecule level by direct stochastic optical-reconstruction microscopy (dSTORM). We show that P2X7 is homogenously dispersed on the plasma membrane as single receptors in quiescent (non-inflammatory condition) microglia. However, upon exposure to the pro-inflammatory agent lipopolysaccharide (LPS), a pathogen-associated molecular pattern (PAMP) from Gram-negative bacteria, combined with ATP or its potent synthetic analog BzATP, P2X7 undergoes significant upregulation and clustering, resulting in the synergistic release of IL-1β. Our findings suggest that the dynamic clustering of P2X7 on the plasma membrane is a crucial mechanism underlying IL-1β secretion.

Results

Design and synthesis of X7-uP

X7-uP was rationally designed by leveraging available X-ray structures of the panda P2X7 receptor (pdP2X7) bound to non-competitive P2X7 antagonists (42). These antagonists bind to an interfacial allosteric binding pocket in pdP2X7, distinct from ATP-binding sites, and accessible from the upper side of the trimeric receptor (42). Due to the trimeric assembly of P2X subunits, three allosteric binding sites are present in P2X7 (Figure 1B). We focused on AZ10606120, a selective antagonist with high-affinity for human (hP2X7) and rat P2X7 (rP2X7), with no effect on other P2X receptors (43-46). The X-ray structure revealed several lysine residues localized in proximity to AZ10606120 (< 15 Å, measured from α-carbon of K72, K81, K82, K110 and K300, and the solvent-exposed hydroxyl of AZ10606120) (Figure 1B inset). Since most of these lysine residues are unique to P2X7 (Figure 1 — figure supplement 1A), we hypothesized that NASA chemistry could selectively label P2X7. We modified AZ10606120 by replacing its solvent-exposed hydroxyethyl group with the reactive *N*-cyanomethyl NASA derivative, allowing a labeling reaction with the ε-amino group of

nearby P2X7 lysine residues, forming a stable amide bond (Figure 1A). We used molecular docking to identify molecule **1** as a promising molecular scaffold built from AZ10606120 (Figure 1 — figure supplement 1B). The distance separating the NASA electrophilic carbon of **1** and each α-carbon of nearby P2X7 residues was compatible with a proximity-driven reaction with rP2X7 (≤ 16.1 Å, Figure 1 — figure supplement 1C), the receptor species used to experimentally validate the approach (see below). Thus, we designed and synthesized **X7-uP**, an extended version of **1**, containing an OEG (olygoethylene glycol) biotin tag (Figure 1C). **X7-uP** is expected to covalently transfer the biotin tag to P2X7, which, in turn, can serve as a versatile platform for subsequent cell surface labeling with commercially available, cell-impermeable biotin-binding protein-conjugated molecular probes, including Alexa 647, suitable for super-resolution microscopy (Figure 1A). **X7-uP** was synthesized as described in Methods (Figure 1 — figure supplement 2).

X7-uP inhibits and biotinylates heterologously expressed rP2X7 in HEK293T cell

To address possible loss of affinity due to chemical modifications of the pharmacophore, we first assessed the ability of **X7-uP** to bind to P2X7 by measuring agonist-evoked current inhibition using whole-cell patch-clamp electrophysiology. In HEK293T cells transiently transfected with rP2X7, we recorded inward currents induced by eight successive applications of 10 μM 2'(3')-*O*-(4-benzoylbenzoyl)ATP (BzATP), a potent P2X7 agonist (Figure 2A). As expected, currents facilitated upon successive BzATP applications, a hallmark feature of P2X7 (47). Application of 1 μM of **X7-uP** for 10 s after washout of the fourth BzATP application did not induce inward currents but strongly inhibited currents induced by co-application for 2 s with BzATP (79.3 ± 5.6%, mean ± standard error of the mean (s.e.m.), n = 4; control without inhibitors: -15.2 ± 4.4%, n = 4), as expected for a potent antagonist. Inhibition was reversible, as BzATP-evoked currents fully restored upon **X7-uP** washout (Figure 2A). Compared to the parental AZ10606120 compound, for which full inhibition was observed (99.7 ± 0.1%, n = 4) at 1 μM (Figure 2A and B), these data suggest that the chemical modification of AZ10606120 has a minimal impact on the inhibition of P2X7 by **X7-uP**.

To test labeling efficiency, HEK293T cells were transiently transfected with c-myc tagged rP2X7 (P2X7c-myc) and incubated at 20°C with 1 μM **X7-uP** for 60 min. **X7-uP** labeling was performed under physiological conditions (1 μM for 10 min at 37°C in FBS-free DMEM, see Methods), followed by extensive washing to remove excess **X7-uP**. After cell lysis, biotinylated proteins were pulled down with NeutrAvidin Agarose, separated on SDS-PAGE, and revealed with an anti-c-myc antibody in Western blot analysis. A strong and unique band was detected in the Western blot at the expected apparent molecular mass of monomeric P2X7c-myc (~75-80 kDa) (Figure 2C). However, this band disappeared upon co-incubation with AZ10606120 (10 μM), or in the absence of **X7-uP** (lane 1), while robust signals corresponding to P2X7c-myc and β-actin expression were still detected in the corresponding input controls (Figure 2C). Similarly, no signal was detected in non-transfected cells treated with **X7-uP** (Figure 2 — figure supplement 1A). To further demonstrate the pharmacological specificity of P2X7 labeling by **X7-uP**, we used another non-competitive P2X7 antagonist, A740003 (10 μM), which targets the same allosteric binding cavity as AZ10606120 in pdP2X7 but is chemically different from AZ10606120 (48). As expected, no labeling was detected when A740003 was co-incubated with **X7-uP** (Figure 2C). Taken together, these data strongly suggest that **X7-uP** biotinylates P2X7 residues by targeting the unique P2X7 allosteric binding site.

We next conducted a kinetic analysis of P2X7 labeling by incubating cells with **X7-uP** at different concentrations and monitoring labeling through quantitative Western blotting analysis. The time course of P2X7 labeling at 1 μM of **X7-uP** is shown in Figure 2C, D, with labeled bands detected as early as 5 min of incubation time. The data were fitted to Eq. (1), derived according to a kinetic model in which an irreversible chemical reaction follows a reversible ligand binding reaction in a large excess of ligand (see Methods) (41), providing the pseudo-first-order reaction rate (k_{app}) of the labeling reaction. Kinetics of labeling carried out at different **X7-uP** concentrations allowed us to plot k_{app} values against **X7-uP** concentrations (Figure 2 — figure supplement 1B-D). The data

were fitted to Eq. (2), providing the labeling rate constant k_L (0.011 ± 0.003 s^{-1}, mean of triplicate ± standard deviation (s.d.)), the dissociation constant K_d (7.3 ± 2.7 μM, mean ± s.d.), and the second-order rate constant (k_L/ K_d = 1.5 × 10^3 $M^{-1}s^{-1}$). The second-order rate constant value was in the same order of magnitude as those of previously described labeling reagents based on NASA chemistry (41).

Next, we determined **X7-uP** labeling yield by quantifying the amount of P2X7c-myc in the supernatant after pulling down biotinylated P2X7c-myc (Figure 2 — figure supplement 2A). This amount, corresponding to unbiotinylated P2X7c-myc, was then compared to the maximal amount of unbiotinylated P2X7c-myc carried out in the absence of **X7-uP**, thus providing labeling yield. Quantitative Western blotting analysis revealed that 65 ± 3% (mean of triplicate ± s.e.m.) of P2X7c-myc were labeled by 1 μM of **X7-uP** for 60 min in HEK293T cells (Figure 2 — figure supplement 2B).

X7-uP labeling is selective for P2X7

Having established the efficacy of P2X7 labeling by Western blot, we next assessed the selectivity of **X7-uP** towards the P2X family. We performed **X7-uP** labeling in HEK293T cells transiently transfected with various fluorescently tagged rat P2X subunits (P2X1 to P2X6). The biotinylated cells were then visualized using Strept-A 647 labeling through confocal microscopy. These P2X subtypes are closely related to P2X7 but are not expected to exhibit the AZ10606120 allosteric site.

As expected, confocal microscopy revealed a strong Alexa 647 fluorescence signal in the periphery of cells expressing only P2X7 tagged with the monomeric Scarlet (mScarlet) fluorescent protein (Figure 3A). In contrast, no Alexa 647 signal was detected in cells transiently transfected with other P2X subunits tagged with GFP, although a strong GFP signal was observed for all constructs, confirming correct expression (Figure 3B and C). Furthermore, co-incubation with AZ10606120 (10 μM) or A740003 (10 μM) during **X7-uP** labeling abolished the Alexa 647 signal, but did not affect mScarlet signal, further confirming the specificity of P2X7 labeling (Figure 3A and C). These data demonstrate the high selectivity of **X7-uP** for P2X7 labeling.

To further validate our method for single-molecule localization microscopy, we employed dSTORM to visualize the fluorescence emission of individual Alexa 647 fluorophores bound to P2X7 expressed on the plasma membrane of HEK293T cells. Our results confirmed the expression of P2X7 at the cell surface, consistent with confocal microscopy data (Figure 3 — figure supplement 1A). Importantly, no emission was detected when labeling was conducted in the presence of AZ10606120 (10 μM), or when Strept-A 647 was added to cells not treated with **X7-uP** (Figure 3 — figure supplement 1B and C), indicating that the observed emission in dSTORM specifically originated from P2X7.

X7-uP labels K82 and K117 in rP2X7

We next identified the labeling site of **X7-uP**. Since it has been shown that the NASA reagent preferentially reacts with the ε-amino group of lysine side chains (41), we individually mutated K82, K110, K117, and K300 into alanine, an amino acid residue that cannot react with NASA, in the P2X7-mScarlet background. These residues were selected based on the predicted proximity of their equivalent positions in pdP2X7 to the electrophilic NASA group of **1** in pdP2X7 (Figure 4A and Figure 1 — figure supplement 1A). We expressed these mutants individually in HEK293T cells and monitored **X7-uP** labeling by quantifying Alexa 647 signals through confocal microscopy. While K110A and K300A mutants did not affect **X7-uP** labeling, where Alexa 647 fluorescence quantification showed comparable levels to that of P2X7-mScarlet (Figure 4C and Figure 4 — figure supplement 1), a significant reduction in Alexa 647 fluorescence was observed for K82A (79.6 ± 1.0 %, n = 154 cells, $P < 0.0001$, *t*-test to the respective control P2X7-mScarlet) and K117A (61.5 ± 2.1%, n = 155 cells, $P < 0.0001$). Importantly, a strong mScarlet signal was detected for all mutants, indicating successful expression of mutants in cells (Figure 4B and Figure 4 — figure supplement 1). Alexa 647 fluorescence reduction at K82A was significantly different from that at

K117A ($P < 0.0001$, *t*-test), suggesting a larger contribution of K82 to **X7-uP** labeling. The double mutant K82A/K117A further reduced the signal by 87.3 ± 0.4% (n = 199 cells, $P < 0.0001$, *t*-test to respective control P2X7-mScarlet, K82A or K117A), without affecting P2X7 expression (Figure 4B and C). To exclude the possibility that introduced mutations affected **X7-uP** binding, we further demonstrated that the double K82A/K117A mutant did not affect the ability of **X7-uP** to inhibit BzATP-evoked currents (Figure 4D and E). These data support the hypothesis that both K82 and K117 are the sites of **X7-uP** labeling in rP2X7.

X7-uP reveals uniform membrane distribution of P2X7 in quiescent BV2 cells

Our data demonstrate the high selectivity of **X7-uP** for P2X7 in HEK293T cells. We next investigated whether its application extends to native P2X7-expressing microglia to reveal endogenous P2X7 expression. We chose BV2 cells, a cultured murine microglia model where the functional expression of P2X7 has been previously documented (26, 27). In addition, the activation of microglia to mimic inflammation can be effectively stimulated *in vitro* using both LPS and ATP (17). Although K117 is not conserved in mouse P2X7, the highly conserved K82 should ensure the successful labeling of mouse P2X7 with **X7-uP** (Figure 1 — figure supplement 1A).

We first confirmed by ELISA assay that, under untreated conditions, BV2 cells are quiescent as they do not release IL-1β (Figure 5A, B). We also confirmed P2X7 expression by Western blot and confocal microscopy following 1 μM **X7-uP** labeling for 10 min in FBS-free DMEM (Figure 5 — figure supplement 1). As observed for HEK293T cells, a strong and unique band was detected using a P2X7 antibody only in the presence of **X7-uP** in the pulldown Western blot, at the excepted apparent molecular mass of monomeric mouse P2X7 (~68 kDa, unglycosylated form; see lanes 3 and 4 in Figure 5 — figure supplement 1A). This band disappeared upon co-incubation with AZ10606120 or A740003, while controls in the supernatant consistently showed endogenous P2X7 expression in all lanes, though non-specific bands were also observed, presumably due to the limited specificity of commercially available P2X7 antibodies (Figure 5 — figure supplement 1B). Quantitative Western blotting analysis revealed that 80 ± 1% (mean of triplicate ± s.e.m.) of total P2X7 were labeled in BV2 cells (Figure 2 — figure supplement 2A and B). Confocal microscopy revealed a strong Alexa 647 fluorescence signal in the periphery of BV2 cells that was reduced upon co-incubation with AZ10606120 or A740003 (Figure 5 — figure supplement 1C and D). Control with Strept-A 647 alone showed an extremely low fluorescence background level (Figure 5 — figure supplement 1C and D), demonstrating high **X7-uP** labeling specificity in BV2 cells.

To assess how BV2 activation affects P2X7 molecular organization, we employed dSTORM to track single fluorophores tagged to endogenous receptors. In this super-resolution technique, each fluorophore blinks several times before becoming silent due to bleaching or reaching a stable dark state. As a result, clusters of detections could result either from multiple blinks of a single receptor or represent the sum of multiple fluorophore emissions from clustered receptors. To quantify nanoscale object properties, we used Metamorph to obtain pixelized global images for global quantification (Figure 5 — figure supplement 2D), and SR-Tesseler, an open-source segmentation framework based on Voronoï tessellation from localized molecule coordinates (49), to analyze cluster properties (Figure 5H and I).

In control untreated condition (quiescent cells), dSTORM revealed punctated images, while no detections occurred without **X7-uP**, further confirming high labeling specificity in BV2 cells (Figure 5D, and Figure 5 — figure supplement 2A and B). Detections are organized into clusters of 44 nm in size (median, 25% percentile 18 nm, 75% percentile 80 nm), with on average 70 ± 15 (mean ± s.e.m.) detections per cluster (n = 4 cells, Figure 5G). Distribution analysis suggests that detections of fluorescent streptavidin conjugates are originating from one single receptor. On average, every P2X7 receptor is separated from its neighbor by a mean inter-cluster distance of 292 ± 5 nm (Figure

5 — figure supplement 2G). These data suggest that P2X7 is homogenously dispersed on the cell surface of quiescent BV2 cells.

Since P2X7 has been suggested to be associated with lipid rafts (20-25), we pre-incubated cells with 15 mM methyl-β-cyclodextrin (MβCD), a lipid-raft disrupting agent, for 15 min, and labeled P2X7 with **X7-uP** after extensive washout to remove remaining MβCD (Figure 5A). MβCD treatment had no effect on IL-1β release, the number of detections per cluster, cluster size, or inter-cluster distance (Figure 5B, F and G, Figure 5 — figure supplement 2C and G). We interpret these results to suggest that disrupting lipid rafts does not alter P2X7 distribution in quiescent BV2 cells.

X7-uP reveals P2X7 clustering and upregulation in activated BV2 cells

We analyzed changes in cluster properties following BV2 activation by LPS and P2X agonists. To reliably correlate P2X7 spatial distribution with the inflammatory response, we labeled the same BV2 cells used for IL-1β release assays with **X7-uP** (Figure 5A). Previous studies have proposed a two-signal, synergistic model for IL-1β release in microglia and other cell types (5, 6, 10, 50-52), where the first signal involves LPS priming, leading to the intracellular accumulation of pro-IL-1β, while the second involves ATP-dependent P2X7 stimulation, promoting caspase-1 activation and the release of mature IL-1β. We confirmed this model by observing robust IL-1β release when BV2 cells were exposed to 1 mg/mL LPS for 24 hours, followed by 1 mM ATP (or 300 mM BzATP) for 30 minutes (LPS+ATP or LPS+BzATP) (Figure 5B). No IL-1β release was detected when ATP or BzATP was applied alone, while LPS alone induced significant release. However, this release was significantly less than that induced by co-treatments, representing only 35% of the release observed with LPS+ATP and 21% with LPS+BzATP (Figure 5B), confirming the synergistic effect. Co-incubation with AZ10606120 or A740003 during agonist exposure reduced IL-1β release to levels observed with LPS alone, demonstrating the role of P2X7 in IL-1β release (Figure 5A and C).

dSTORM images following treatments are shown in Figure 5D. Global single-molecule labeling on the cell surface was significantly more pronounced in cells treated with LPS+ATP or LPS+BzATP, and to a lesser extent, though not significantly, in those treated with LPS alone compared to untreated control (Figure 5E). Similar results were obtained using confocal microscopy, although the effect of LPS alone was significant (Figure 5 — figure supplement 3). Neither ATP nor BzATP application alone affected the number of detections per cluster, cluster size, or inter-cluster distance. At the cluster level, both LPS and LPS+ATP or LPS+BzATP treatments increased the number of detections per cluster (Figure 5E and G and Figure 5 — figure supplement 2D and E), with no change in inter-cluster distance or average intensity per sub-pixel (Figure 5 — figure supplement 2F and G), indicating no increase in detection density per pixel. On pixelized images, larger clusters (area greater than 0.025 mm^2, insert Figure 5F) emerged following LPS treatment, with or without agonists. Tessellation analysis revealed that the number of fluorophores within clusters significantly increased from ~1.5 in untreated cells to 4.1 ± 0.4 for LPS, 4.9 ± 0.5 for LPS+ATP, and 5.2 ± 0.5 for LPS+BzATP (Figure 5H and I). These data demonstrate that pro-inflammatory conditions induce P2X7 clustering by upregulating the average number of P2X7 receptors within clusters, increasing it from one to three, and favoring the formation of larger clusters (Figure 6). The strong P2X7 clustering induced by the combination of LPS and P2X7 agonists mirrors IL-1β secretion.

Discussion

We present a rapid and efficient method for the selective labeling of P2X7 in native cells. This approach allowed us to uncover a nanoscale redistribution mechanism of individual endogenous P2X7 receptors on the plasma membrane of activated BV2 microglial cells, leading to the synergistic release of the pro-inflammatory cytokine IL-1β.

Our strategy employs an affinity-guided approach, through which we developed **X7-uP**, a selective P2X7 biotinylating reagent that covalently attaches a biotin tag to lysine residues on native P2X7. In rat P2X7 (rP2X7), we identified two lysine residues as labeling sites: K82, a highly conserved residue unique to P2X7, and K117, a residue present only in rP2X7. We found that K82 is the primary labeling site in rP2X7, and given that K117 is absent in mouse P2X7, it is likely that K82 is the only labeled site in BV2-expressing P2X7.

We demonstrate the effectiveness of **X7-uP** in both heterologous and native expression systems. Compared to existing methods, **X7-uP** offers several advantages. First, it combines *N*-cyanomethyl NASA chemistry with the high-affinity AZ10606120 ligand, enabling rapid labeling in microglia (within 10 min) at a low **X7-uP** concentration (1 μM) in physiological-like buffer (e.g., FBS-free DMEM). Second, because AZ10606120 binds to a unique P2X7 allosteric site (48), **X7-uP** is highly selective for P2X7, with no labeling observed in cells expressing other P2X or when specific P2X7 antagonists are present. This selectivity makes **X7-uP** particularly suitable for detecting P2X7 in native tissues, addressing the specificity issues seen with available antibodies (39). Third, **X7-uP** provides a versatile platform to deliver various probes to P2X7, including those for pulldown assays and super-resolution imaging. The strong biotin-streptavidin (or neutravidin) interaction ensures specificity and stability, two crucial criteria for biochemical assays and cell imaging.

Our results not only confirm P2X7 expression in microglia, as previously reported (6, 26-33), but also reveal its nanoscale localization at the cell surface using dSTORM. In quiescent cells, P2X7 is evenly distributed across the plasma membrane, likely as individual receptors with an average nearest-neighbor distance of ~300 nm, indicating the absence of clustering. To test whether P2X7 associates with cholesterol-enriched lipid rafts, we pre-treated cells with MβCD, a cholesterol-depleting agent that perturbs lipid rafts. This treatment did not affect P2X7 distribution, although we have previously shown in HEK293T cells that MβCD increases P2X7 single-channel mean open time without altering unitary conductance (53). These findings suggest that in quiescent BV2 microglial cells, perturbating lipid rafts does not alter the uniform distribution of individual P2X7 receptors, which likely reside within cholesterol-enriched nanodomains.

Under inflammatory conditions, we observed significant nanoscale reorganization of P2X7. Both LPS and ATP (orBzATP) trigger P2X7 upregulation and clustering, increasing the overall number of surface receptors and the number of receptors per cluster, from one to three (Figure 6). By labeling BV2 cells with **X7-uP** shortly after IL-1β release, we were able to correlate the nanoscale distribution of P2X7 with the functional state of BV2 cells, consistent with the two-signal, synergistic model for IL-1β secretion observed in microglia and other cell types (5, 6, 10, 50-52). In this model, LPS priming leads to intracellular accumulation of pro-IL-1β, while ATP stimulation activates P2X7, triggering NLRP3 inflammasome activation and the subsequent release of mature IL-1β. Although the mechanism behind the overall increase in surface receptors remains unclear, a recent study suggests that the a1 subunit of the Na^+/K^+-ATPase (NKAα1) forms a complex with P2X7 in microglia, including BV2 cells, and that LPS+ATP induces NKAα1 internalization (17). This internalization appears to release P2X7 from NKAα1, allowing P2X7 to exist in its free form. We speculate that the internalization of NKAα1 induced by both LPS and ATP exposes previously masked P2X7 sites, including the allosteric AZ10606120 sites, thus making them accessible for **X7-uP** labeling.

In sequence, the first priming step induced by LPS triggers P2X7 clustering and tends to increase the number of cell-surface receptors. This modest increase in P2X7 density may explain the lack of functional upregulation in the amplitude of the P2X7 current component observed in BV2 cells following LPS treatment (26, 27). The second step, triggered by ATP exposure, further elevates surface receptor levels and activates the P2X7-mediated NLRP3 inflammasome, which cleaves pro-IL-1β into its mature form and facilitates its release. Previous evidence suggests that P2X7 and NLRP3 co-localize in mouse microglia (54), indicating that NLRP3 may reside beneath P2X7 clusters. We propose that the spatial reorganization and clustering of P2X7 during the LPS-induced priming phase at sites of active inflammation is an efficient mechanism to ensure synergistic IL-1β secretion in response to ATP. This clustering mechanism represents a finely tuned regulatory process that effectively links PAMP-induced signaling to DAMP-evoked responses.

In conclusion, **X7-uP** is a powerful tool for visualizing P2X7 localization at the nanoscale on the cell surface of BV2 cells. We anticipate that **X7-uP** will become a valuable molecular probe for investigating P2X7 organization in other native cell types, such as macrophages, and for resolving the ongoing debate about P2X7 expression in neurons (55, 56).

Materials and Methods

Chemical synthesis

All chemicals were purchased from Sigma-Aldrich, Acros Organics or Alfa Aesar in analytical grade. An agilent MM-ESI-ACI-SQ MSD 1200 SL spectrometer or an Agilant LC-MS Agilent RRLC 1200SL/ESI QTof 6520 was used for ESI analysis. ^{1}H NMR and ^{13}C NMR spectra were recorded at 400 or 700, and 100 or 175 MHz, respectively, using the following NMR Bruker instruments: a 400 MHz spectrometer equipped with an Avance III console and a BBO H/F z-gradient probe or a 700 MHz spectrometer equipped with a TCI z-gradient cryoprobe and an Avance III-HD console. Coupling constants (*J*) are quoted in hertz (Hz) and chemical shifts (δ) are given in parts per million (ppm) using the residue solvent peaks ($CDCl_3$: 7.26 ppm, MeOD: 3.31 ppm, DMSO-d_6: 2.50 ppm for ^{1}H NMR and $CDCl_3$: 77.16 ppm, MeOD: 49 ppm, DMSO-d_6: 39.52 ppm for ^{13}C NMR). The attributions are given in the following manner: chemical shift followed by the multiplicity in parenthesis (s, d, t, q, m, dd, dt, br corresponding respectively to singlet, doublet, triplet, quadruplet, multiplet, doublet of a doublet, doublet of a triplet, broad; number of protons and coupling constant in Hz).

HPLC analyses were performed on a Waters® high-performance chromatography system (1525 pump, 2996 detector) equipped with a Thermo Betabasics 5-micron analytical column (4.6, 250 nm). A gradient solution was applied, progressing from 100% mQ H_2O acidified with 0.01% TFA to 100% acetonitrile over 30 min, followed by 10 min at 100% acetonitrile. HPLC purifications were carried out on a Waters® high-performance chromatography system (600 double body pump, 2996 detector) equipped with a Thermo Betabasics 5-micron semi-preparative column (10, 250 nm), using the same gradient as described above.

5-aminoquinolin-2(1H)-one (3):

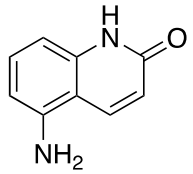

3

To a solution of 5-nitroquinolin-2(1H)-one (**2**) (1 g, 5.26 mmol, 1 eq.) dissolved in N,N-dimethylformamide (DMF, 40 mL) froze at -196°C was added dry palladium on activated coal (10%) (448 mg, 2.21 mmol, 0.8 eq.). Solution was let to warm up at room temperature and gaseous dihydrogen was bubbled in the solution for 5 minutes. Reaction was then let under dihydrogen atmosphere and stirred for 16 h. Crude product was then filtrated on a celite pad. The pad was further rinsed with DMF (100 mL) and the filtration product was evaporated to yield a grey solid (825 mg, 98 %).

^{1}H NMR (400 MHz, MeOD): δ 8.19 (dd, *J* = 9.7, 1.0 Hz, 1H), 7.26 (m, 1H), 6.63 (dt, *J* = 8.1, 1.0 Hz, 1H), 6.55 (dd, *J* = 8.1, 1.0 Hz, 1H), 6.47 (d, *J* = 9.7 Hz, 1H). See Figure 1 — figure supplement 3 for spectrum.

2-(adamantan-1-yl)acetyl chloride (4):

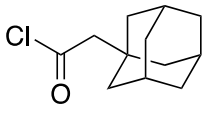

4

2-(1-adamantyl)acetic acid (1.1 g, 5.67 mmol, 1 eq.) was placed in an oven-dried flask equipped with a reflux. Thionyl chloride (10 mL) was added and the solution was heat to reflux under argon atmosphere for 3 h. Solvent was then evaporated and the resulting yellow oil was further dried under vacuum. Obtained compound was immediately used in the next step.

2-(adamantan-1-yl)-*N*-(2-oxo-1,2-dihydroquinolin-5-yl)acetamide (5):

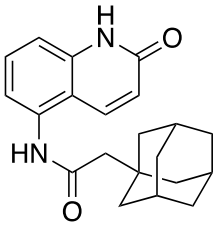

5

To a stirred solution of 5-aminoquinolin-2(1H)-one (**3**) (825 mg, 5.15 mmol, 1 eq.) in anhydrous tetrahydrofuran (THF) was added freshly distilled triethylamine (1,11 mL, 8,24 mmol, 1,6 eq.). The mixture was cooled to 0°C and a solution of 2-(-adamantan-1-yl)acetyl chloride (1.2 g, 5.67 mmol, 1.1 eq) (**4**) dissolved in dry THF (5 mL) was added dropwise over the course of 15 minutes to form a grey solution. The solution was kept at 0°C for 1 h and brought to 20 °C for 2 more hours. The solution was then evaporated and the obtained solid was rinsed 3 times with CH_2Cl_2 (50 mL). The solid was further dried to yield the expected compound as a grey solid (1.4 g, 81 %). The product was then used without further purification.

^{1}H NMR (400 MHz, MeOD): δ 8.06 (dd, *J* = 9.8, 0.8 Hz, 1H), 7.58 – 7.54 (m, 1H), 7.33 (dd, *J* = 7.8, 1.1 Hz, 1H), 7.26 (m, 1H), 6.65 (d, *J* = 9.8 Hz, 1H), 2.26 (s, 2H), 2.03 (m, 3H), 1.86 – 1.70 (m, 12H). See Figure 1 — figure supplement 4 for spectrum.

2-(adamantan-1-yl)-*N*-(2-chloroquinolin-5-yl)acetamide (6)

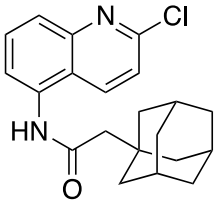

6

To a stirred solution of 2-(adamantan-1-yl)-*N*-(2-oxo-1,2-dihydroquinolin-5-yl)acetamide (**5**) (725 mg, 2.15 mmol, 1 eq.) dissolved in 1,2-dichloroethane (10 mL) was added freshly distilled $POCl_3$ (618 μL, 6.45 mmol, 3 eq.). The solution was brought to reflux for 16 h and the solvent was evaporated. Crude product was dissolved in CH_2Cl_2, filtrated and evaporated to yield the expected compound as an orange solid (760 mg, 99 %).

^{1}H NMR (400 MHz, MeOD): δ 8.43 (dd, *J* = 8.8, 0.8 Hz, 1H), 7.87 – 7.79 (m, 2H), 7.72 (dd, *J* = 7.2, 1.5 Hz, 1H), 7.59 – 7.55 (m, 1H), 2.30 (s, 2H), 2.03 (m, 3H), 1.86 – 1.72 (m, 12H). See Figure 1 — figure supplement 5 for spectrum.

2-(adamantan-1-yl)-*N*-(2-((2-aminoethyl)amino)quinolin-5-yl)acetamide (7):

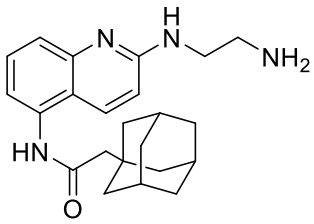

7

To a stirred solution of 2-(adamantan-1-yl)-N-(2-chloroquinolin-5-yl)acetamide (**6**) (488 mg, 1.36 mmol, 1 eq.) in freshly distilled ethanol (10 mL) was added dry K_2CO_3 (376 mg, 2.72 mmol, 2 eq.)

and anhydrous ethylene diamine (4.5 mL, 68 mmol, 50 eq.). The mixture was stirred for 48 h at reflux. The solution was evaporated and subsequently extracted with 3 × 50 mL CH_2Cl_2. Organic layers were combined, washed with 25 mL of brine and dried over $MgSO_4$, filtered and evaporated. The crude extract was retaken in a minimum of CH_2Cl_2 and diethyl ether was added dropwise until apparition of opalescence. Heptane was then slowly added to precipitate the pure product (262 mg, 51 %) as a yellow solid.

^{1}H NMR (400 MHz, MeOD): δ 7.96 (d, *J* = 9.2 Hz, 1H), 7.56 – 7.46 (m, 2H), 7.23 (dd, *J* = 7.2, 1.4 Hz, 1H), 6.80 (d, *J* = 9.2 Hz, 1H), 3.57 (t, *J* = 6.2 Hz, 2H), 2.91 (t, *J* = 6.2 Hz, 2H), 2.25 (s, 2H), 2.03 (m, 3H), 1.87 – 1.68 (m, 12H). See Figure 1 — figure supplement 6 for spectrum.

_N_-(2-((5-(2-(adamantan-1-yl)acetamido)quinolin-2-yl)amino)ethyl)-4-sulfamoylbenzamide (8):

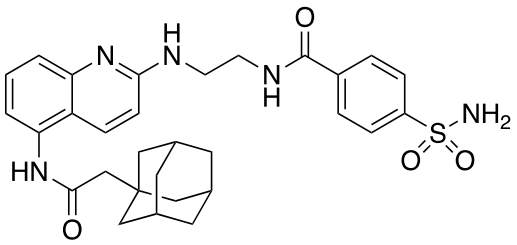

8

To a stirred solution of 2-(adamantan-1-yl)-N-(2-((2-aminoethyl)amino)quinolin-5-yl)acetamide (**7**) (105 mg, 0.28 mmol, 1 eq.) in dry DMF (2.5 mL) is added 4-sulfamoylbenzoic acid (67 mg, 0.33 mmol, 1.2 eq.), 1-Hydroxybenzotriazole (45 mg, 0.33 mmol, 1.2 eq.) and DIEA (129 µL, 0.75 mmol, 2.7 eq.). The solution was cooled down to 0°C and EDC (64 mg, 0.33 mmol, 1.2 eq.) was added. The mixture was then slowly warmed up to 20°C, and stirred at 20°C for 18 h. Solvent was evaporated and the crude product was purified by invert phase flash chromatography (gradient acetonitrile: H_2O (0.1 % TFA), 0:1 to 1:0 over 30 min, retention time: 16.2 min) to yield pure compounds as an orange solid (100 mg, 64 %).

^{1}H NMR (400 MHz, MeOD): δ 8.19 (d, *J* = 9.5 Hz, 1H), 8.02 – 7.91 (m, 4H), 7.70 (m, 2H), 7.45 (dd, *J* = 7.5, 1.3 Hz, 1H), 7.04 (d, *J* = 9.5 Hz, 1H), 3.83 (t, *J* = 6.2 Hz, 2H), 3.73 (t, *J* = 6.2 Hz, 2H), 2.28 (s, 2H), 2.02 (s, 3H), 1.88 – 1.68 (m, 12H).

^{13}C NMR (100 MHz, MeOD): δ 173.92, 169.94, 165.28, 160.81, 156.37, 148.36, 138.62, 136.24, 133.03, 129.52, 127.77, 122.82, 119.63, 119.19, 114.59, 65.67, 55.16, 52.36, 44.52, 38.31, 34.83, 30.50. See Figure 1 — figure supplement 7 for spectra.

MS (ESI): m/z [M^+] calculated for $C_{30}H_{36}N_5O_4S^+$: 562.2483, found 562.2516.

***tert*-butyl (15-((4-((2-((5-(2-(adamantan-1-yl)acetamido)quinolin-2-yl)amino)ethyl)carbamoyl)phenyl)sulfonamido)-15-oxo-3,6,9,12-tetraoxapentadecyl)carbamate (10):**

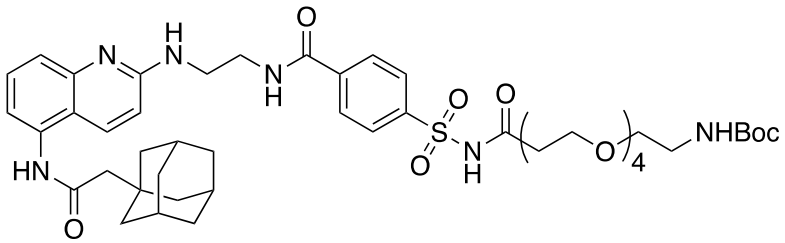

10

To a stirred solution of *N*-(2-((5-(2-(adamantan-1-yl)acetamido)quinolin-2-yl)amino)ethyl)-4-sulfamoylbenzamide (**8**) (43 mg, 76 µmol, 1 eq.) in dry DMF (1 mL) was added COOH-OEG4-Boc (**9**) (33.6 mg, 92 µmol, 1.2 eq.), DIEA (33 µL, 191 µmol, 2.5 eq.) and DMAP (2 mg, 15 µmol, 0.2

eq.). Solution was cooled down to 0°C and EDC was added (17.6 mg, 92 μmol, 1.2 eq.). Solution was let to slowly warm up to 20°C for 16 h. Every 24 h during 72 h was added 1 eq. of carboxylic acid, 1 eq. of EDC and 2 eq. of DIEA at 0°C. Solvent was then evaporated and 50 mL of a 1:1 CH_2Cl_2:H_2O solution was added. Organic layer was extracted with 2 × 20 mL of CH_2Cl_2. Organics layers were then combined, dry over $MgSO_4$, filtered and evaporated. Compound was purified by HPLC purification (acetonitrile:H_2O (0.1% TFA), 0:1 to 1:0 over 30 min, retention time: 17.7 min). Pure fractions were combined, extracted with 3 × 20 mL, dry over $MgSO_4$ and evaporated to yield pure compound as a dark orange oil (57 mg, 82 %).

^{1}H NMR (400 MHz, $CDCl_3$): δ 8.20 (m, 1H), 8.01 (m, 4H), 7.42 (m, 3H), 6.85 (s, 1H), 3.79 (m, 2H), 3.60 (m, 18H), 3.26 (s, 2H), 2.48 (s, 2H), 2.22 (s, 2H), 1.98 (s, 3H), 1.77 – 1.59 (m, 12H), 1.41 (s, 9H).

^{13}C NMR (100 MHz, CDCl3): δ 171.08, 170.38, 168.12, 166.33, 156.37, 153.55, 139.80, 137.58, 134.55, 133.23, 128.28, 127.87, 121.02, 115.21, 113.45, 108.43, 79.43, 70.45, 70.38, 70.22, 70.13, 66.13, 53.42, 51.57, 42.68, 36.69, 33.47, 28.51. See Figure 1 — figure supplement 8 for spectra.

_N_-(2-((5-(2-(adamantan-1-yl)acetamido)quinolin-2-yl)amino)ethyl)-4-(_N_-(17-oxo-21-((3a_R_,4_R_,6a_S_)-2-oxohexahydro-1_H_-thieno[3,4-_d_]imidazol-4-yl)-4,7,10,13-tetraoxa-16-azahenicosanoyl)sulfamoyl)benzamide (11):

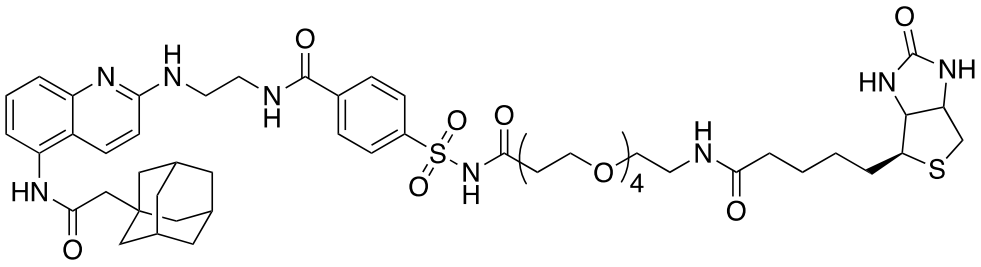

11

To a stirred solution tert-butyl (15-((4-((2-((5-(2-(adamantan-1-yl)acetamido)quinolin-2-yl)amino)ethyl)carbamoyl)phenyl)sulfonamido)-15-oxo-3,6,9,12-tetraoxapentadecyl)carbamate (**10**) (7.6 mg, 8 μmol, 1 eq.) in 700 μl of CH_2Cl_2 was added 100 μl of TFA and the solution was left under argon for 1 h at 20°C. After completed deprotection of the amine (confirmed by HPLC), solvent was evaporated and the residue was further dried by 3 coevaporation with anhydrous toluene (5 mL). Anhydrous DMF was then added in the flask (1 mL), followed by N-methylmorpholine (2 μL, 17 μmol, 2 eq.), biotin (3 mg, 13 μmol, 1.5 eq.) and 4-(4,6-dimethoxy-1,3,5-triazin-2-yl)-4-methyl-morpholinium chloride (DMTMM, 3.4 mg, 13 μmol, 1.5 eq.). Solution was left 2 h at 20°C. Solvent was then evaporated and the pure product was obtained by HPLC purification (acetonitrile: H_2O (0.1% TFA), 0:1 to 1:0 over 30 min, retention time: 18.1 min) to yield an orange solid (7 mg, 80 %).

^{1}H NMR (500 MHz, MeOD): δ 10.01 (s, 1H), 9.01 (br, 1H), 8.29 (s, 1H), 8.07 – 7.96 (m, 4H), 7.82 (t, J = 5.6 Hz, 1H), 7.76 – 7.69 (br, 1H), 7.60 (br, 1H), 7.09, (s, 1H), 6.41 (s, 1H), 6.36 (s, 1H), 4.31, (dd, J = 7.6, 4.2 Hz, 1H), 4.13 (dd, J = 7.6, 4.4 Hz, 1H), 3.76 (br, 2H), 3.64 (br, 2H), 3.55 – 3.35 (m, 16H), 3.18 (q, J = 6.2 Hz, 2H), 3.12 – 3.07 (m, 1H), 2.82 (dd, J = 12.6, 5.3 Hz, 1H), 2.58 (J = 12.6, 2H), 2.21 (m, 2H), 2.06 (t, J = 7.3 Hz, 2H), 1.97 (s, 3H) 1.72 – 1.57 (m, 12H), 1.53 – 1.41 (m, 3H), 1.35 – 1.23 (m, 3H).

^{13}C NMR (100 MHz, MeOD): δ 174.74, 172.09, 170.58, 168.23, 164.72, 159.59, 153.15, 137.88, 136.88, 135.05, 132.40, 128.07, 127.70, 122.07, 116.79, 115.21, 113.51, 70.14, 70.12, 70.00, 69.17, 65.80, 61.98, 60.26, 55.58, 50.55, 42.46, 39.67, 38.97, 36.48, 35.33, 33.05, 28.79, 28.33, 28.09, 25.44. See Figure 1 — figure supplement 9 for spectra.

***N*-(2-((5-(2-(adamantan-1-yl)acetamido)quinolin-2- yl)amino)ethyl)-4-(*N*-(cyanomethyl)-*N*-(17-oxo-21-((3a*R*,4*R*,6a*S*)-2-oxo- hexahydro-1*H*-thieno[3,4-*d*]imidazol-4-yl)-4,7,10,13-tetraoxa-16-azahenico- sanoyl)sulfamoyl)benzamide (X7-uP):**

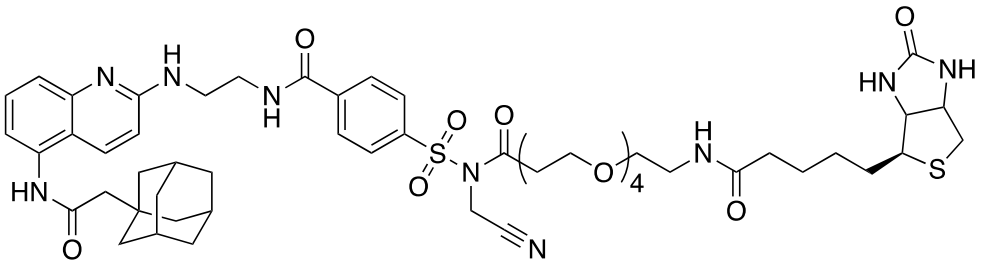

X7-uP

To a stirred solution of N-(2-((5-(2-(adamantan-1-yl)acetamido)quinolin-2-yl)amino)ethyl)-4-(N-(17-oxo-21-((3aR,4R,6aS)-2-oxohexahydro-1H-thieno[3,4-d]imidazol-4-yl)-4,7,10,13-tetraoxa-16-azahenicosanoyl)sulfamoyl)benzamide (**11**) (4 mg, 4 μmol, 1 eq.), previously dried with 5 coevaporation with anhydrous toluene (5 mL), in dried DMF (0.5 mL) was added freshly distilled DIEA (32 μl, 190 μmol, 50 eq.) and iodoacetonitrile (13 μl, 190 μmol, 50 eq.). The latter was dried using alumina plug prior use. The solution was stirred for 16 h at 20°C in the dark and solvent was then evaporated. Pure compound was obtained by HPLC purification (acetonitrile: H_2O (0.1% TFA), 0:1 to 1:0 over 30 min, retention time: 19.1 min) to yield a brown solid (3.3 mg, 80 %).

^{1}H NMR (700 MHz, DMSO): δ 10.02 (s, 1H), 9.08 (br, 1H), 8.29 (s, 1H), 8.14 (d, *J* = 8.3 Hz, 2H), 8.08 (d, *J* = 8.3 Hz, 2H), 7.83 (t, *J* = 5.6 Hz, 1H), 7.76 – 7.72 (br, 1H), 7.60 (br, 1H), 7.09 (s, 1H), 6.42 (s, 1H), 6.37 (s, 1H), 5.02 (s, 2H), 4.31 (dd, *J* = 7.8, 5.0 Hz, 1H), 4.13 (dd, *J* = 7.7, 4.4 Hz, 1H), 3.77 (s, 2H), 3.66 (s, 2H), 3.60 (t, *J* = 6.1 Hz, 2H), 3.53 – 3.42 (m, 12H), 3.39 (t, *J* = 6.0 Hz, 2H), 3.18 (q, *J* = 6.0 Hz, 2H), 3.12 – 3.07 (m, 1H), 2.94 (t, *J* = 6.1 Hz, 2H), 2.82 (dd, *J* = 12.6, 5.1 Hz, 1H), 2.58 (d, *J* = 12.6 Hz, 2H), 2.22 (m, 2H), 2.07 (t, *J* = 7.4 Hz, 2H), 1.97 (s, 3H), 1.73 – 1.58 (m, 12H), 1.53 – 1.43 (m, 4H), 1.34 – 1.23 (m, 2H).

^{13}C NMR (175 MHz, DMSO): δ 170.91, 169.04, 168.67, 164.13, 161.47, 161.06, 156.95, 156.77, 138.73, 137.84, 133.90, 129.02, 128.80, 127.17, 126.67, 116.81, 116.40, 114.96, 114.70, 68.52, 68.47, 68.44, 68.42, 68.31, 68.27, 63.96, 59.78, 57.94, 54.15, 53.63, 48.88, 40.83, 38.72, 37.15, 35.13, 34.63, 34.52, 33.82, 32.69, 31.52, 29.50, 29.42, 26.92, 26.78, 26.76, 23.99. See Figure 1 — figure supplement 10 for spectra.

MS (ESI): m/z [M+] calculated for $C_{53}H_{71}N_9O_{11}S_2^+$: 1074.4787, found 1074.4797.

Molecular modelling

The P2X7 structure resolved with the allosteric inhibitor AZ10606120 was retrieved form the Protein Data Bank (PDB, code 5U1W) (48). The inhibitor was removed, and docking simulations were performed using AutoDock Vina 1.5.6. A 30 Å box centered on the quinoline core of AZ10606120 was used for docking, set before ligand removal. The cartoon shown in Figure 6 was created using tetrameric biotin-bound streptavidin (PDB code 1MK5) and rP2X7 (PDB code 6U9W). Tetrameric biotin-bound streptavidin was positioned relative to K82, using the maximum 18.5 Å distance between the α-carbon of K82 and the carboxylate carbon of the bound biotin.

Cell culture and transfection

HEK293T cells (ATCC) and mouse BV2 microglia cells (kind gift of Dr. R. Schlichter, Institute of Cellular and Integrative Neuroscience, University of Strasbourg, France) were cultured in high-glucose Dulbecco's modified Eagle's medium (DMEM ref. 31966-021) supplemented with 10% (v/v) heat-inactivated fetal bovine serum (FBS), 100 units/mL penicillin and 100 μg/mL streptomycin (Gibco Life Technologies, USA). Cells were grown at 37°C in a humidified cell incubator with 5% CO_2.

For transfection, cells were grown to 70-80% confluence, and the calcium phosphate precipitation method was employed. The cDNA encoding rat P2X7-mScarlet (57), P2X1-GFP, P2X2-GFP, P2X3-GFP, P2X4-GFP, P2X5-GFP, or P2X6-GFP (all kind gifts from Dr. F. Rassendren, Institut de Génomique Fonctionelle, University of Montpellier, France) were contained within pcDNA3.1(+) plasmids (Invitrogen, USA). rP2X7-myc was obtained as previously described (53). 24 h after transfection, the medium was replaced with fresh medium. For whole-cell patch-clamp experiments, cells were co-transfected with the rP2X7 construct (0.8 μg) and an eGFP (0.3 μg) which allowed to identify cells that had undergone efficient transfection. For biochemical experiments, each 100 mm dish was transfected with P2X7-myc construct (10 μg). For confocal imaging and dSTORM experiments, HEK293T cells were transfected with 1 μg of the indicated construct.

Mutagenesis

Site-directed mutations were introduced into the P2X7-mScarlet cDNA in the pcDNA3.1(+) using KAPA HiFi HotStart PCR kit (Cliniscience, France) as previously described (58). All mutations were confirmed by DNA sequencing.

Electrophysiology patch-clamp

Electrophysiological recordings in whole-cell configuration were carried out as previously described (53). Briefly, patch pipettes were pulled from borosilicate glass capillaries and microforged to yield a resistance of 3-5 MΩ. Cells were voltage-clamped to -60 mV using EPC10 USB amplifier (HEKA, Reutlingen, Germany), and data were recorded with PATCHMASTER software (version V2X90.5). Ligands were applied via a perfusion system, using three capillary tubes placed directly over the cell of interest.

2′(3′)-O-(4-benzoylbenzoyl) adenosine 5′-triphosphate (BzATP) (triethylammonium salt, Alomone labs, Israel) was used as P2X7 agonist at a concentration of 10 μM. AZ10606120 and **X7-uP** were used at the indicated concentrations. BzATP was dissolved in Normal Extracellular Solution (NES), containing 140 mM NaCl, 2.8 mM KCl, 1 mM CaCl2, 0.1 mM MgCl2, 10 mM HEPES, and 10 mM glucose, with a pH of 7.32–7.33. AZ10606120 and **X7-uP** were prepared as concentrated stocks in DMSO and diluted in NES to the desired working concentration (< 0.1% DMSO). Only one cell was patched per coverslip.

Labeling reaction with X7-uP

X7-uP was stored as a DMSO stock solution (24.9 mM) and diluted in FBS-free DMEM to achieve the desired working concentration for labeling (< 0.1% DMSO). After three washing steps with freshly prepared sterile-filtered PBS+ buffer (containing 137 mM NaCl, 2.68 mM KCl, 10 mM Na_2HPO_4, 1.76 mM KH_2PO_4, 1 mM $MgCl_2$ and 0.4 mM $CaCl_2$), cells were incubated with **X7-uP** diluted in FBS-free DMEM for the indicated time at 37°C. Following incubation, cells were washed three times with PBS+ buffer and treated as indicated. For confocal and dSTORM experiments, biotinylated cells were incubated with 1 μg/mL of Strept-A 647 (S21374, Invitrogen, USA) for 10 min in PBS+ buffer containing 1% bovine serum albumin (BSA) at 37°C. After three additional washes with PBS+ buffer, cells were fixed as described below.

Pull Down, SDS-PAGE and Western blot

Cells were solubilized by vortexing in a lysis buffer (20 mM HEPES, 100 mM NaCl, 1 % Triton-X, 5 mM EDTA, 1 % protease inhibitor (Thermo Fischer, Waltham, MA, USA)) at 4°C for 90 min. Following centrifugation (14,000 rpm, 10 min), supernatants were collected, mixed with the NuPAGE LDS loading buffer (Thermo Fisher) containing 70 mM dithiothreitol (DTT), boiled for 10 min, and run on a NuPAGE Novex Bis-Tris 4%-12% (Thermo Fischer, USA) in MOPS buffer. Proteins were transferred to a nitrocellulose membrane using semi-wet transfer (TransBlot Turbo system, BioRad, CA, USA), and the membrane was blocked for 30 min in TPBS buffer (PBS buffer supplemented with 1% milk powder, 0.5% BSA and 0.05 % Tween-20). The membrane was then incubated overnight at 4 °C under gentle agitation with primary antibodies: 1:500 anti-c-Myc mouse

antibody (13-2500, Invitrogen, Thermo Fischer), 1:500 rabbit anti-P2X7 antibody (APR-008, Alomone Labs, Israel), or mouse 1:5,000 anti-β-actin (A5441, Sigma Aldrich). Proteins were visualized using 1:10,000 horseradish peroxidase-conjugated secondary antibodies directed against mouse or rabbit (NA9310, GE Life Sciences and 31460, Invitrogen, respectively) and a chemiluminescent substrate (Amersham ECL Select Western Blotting Detection, Ge Life Sciences, MA, USA) on an Imager 600 (Amersham, IL, USA).
For pull-down experiments, solubilized cells (as described above) were incubated overnight at 4 °C under gentle agitation with Pierce NeutrAvidine agarose resin (29200, Thermo Fischer). Samples preparation and Western blotting was carried out as described above.

Coverslip preparation

For confocal imaging and super-resolution experiments, coverslips (0117580, No. 1.5H, Marenfield, Germany) were cleaned by incubation in freshly made piranha solution (H_2SO_4:H_2O_2 50% 3:1) at 60°C for 30 min. The cleaning solution was replaced with fresh piranha solution, and the coverslips were sonicated for an additional 30 min. After discarding the piranha solution, coverslips were washed 10 times with ultra-pure water and sonicated in ultrapure water (10 × 3 min each) to ensure complete removal of any cleaning residue. Coverslips were then dispatched in 12-well plates and exposed to UV light for 30 min. For HEK293T cells, the coverslips were treated with poly-L-lysine for 1 h at 37°C and subsequently washed with ultra-pure water before use. For BV2 cells, no treatment with poly-L-lysine was performed.

BV-2 microglia stimulation

BV2 microglia cells were seeded on treated coverslips (as described above) in a 12-well plate containing standard DMEM medium with 10% FBS. After 24h, cells were incubated in DMEM medium with 1% FBS for 24 h, either left untreated or treated with *Escherichia coli* O111:B4 LPS (1 ng/mL, ref. L2630, Sigma Aldrich, USA). After washing once with freshly prepared sterile-filtered PBS+, cells were incubated in PBS+, either in the absence (vehicle) or supplemented with 1 mM adenosine 5′-triphosphate (ATP disodium salt hydrate, ref. A7699, Sigma Aldrich) for 30 min, 300 μM BzATP for 30 min, or 15 mM MbCD (Sigma Aldrich, USA) for 15 min at 37°C in a humidified cell incubator with 5% CO_2. After treatments, supernatants were collected for the IL-1β ELISA assay, and cells were labeled with **X7-uP** as described above.

ELISA assay

IL-1β levels were measured using the IL-1β Mouse Uncoated ELISA Kit (ref. 88-7013, Invitrogen, USA) following the manufacturer's protocol. Developed plates were read using a SAFAS Monaco plate reader with SP2000 version 7 software.

Cell fixation

Cells were fixed by 4% paraformaldehyde (PFA) in PBS, pH 8.0 for 20 min at 20°C. Fixed cells were then washed three times and incubated with fresh PBS buffer for 3 × 5 min, followed by incubation in 100 mM glycine (in PBS buffer) for 15 min at 20°C. After three washes, cells were stored at 4°C until use. All washing steps were performed with freshly made, sterile-filtered PBS buffer.

Cytochemistry

For confocal imaging, coverslips containing fixed cells were treated with 4 μg/mL of Hoechst 33342 pentahydrate (bis-benzimide) (H21491, Molecular Probes, Life Technologies, USA) in PBS buffer for 10 min. The staining solution was discarded, and coverslips were washed three times with PBS buffer, rinsed with ultra-pure water, mounted on microscopy slides with the Prolong Gold Antifade (P36930, Invitrogen, USA), and allowed to dry overnight in the dark before use.

For confocal imaging of BV2 cells shown in Figure 5 — figure supplement 3, coverslips were rinsed with ultra-pure water, mounted on microscopy slides using the Prolong Diamond Antifade with DAPI (P36962, Invitrogen, USA), and allowed to dry overnight in the dark before use.

For dSTORM experiments in HEK293T cells, coverslips were incubated at room temperature for 6 minutes in a PBS solution containing 1:5,000 fluorescent microspheres (Tetraspeck, Invitrogen, USA) as fiducial markers for lateral drift correction during image reconstruction, rinsed with ultra-pure water, mounted on microscopy slides on a Vectashield® H-1000 (Vector Laboratories, USA) containing a 50 mM TRIS-glycerol (obtained by diluting 5% v/v TRIS pH 8.0 in glycerol and filtered on 0.22 μm filter) in a 1:4 ratio, and sealed using dental cement (Picodent, Germany) (59).

For dSTORM experiments in BV2 cells, coverslips were first incubated at room temperature for 6 minutes in a PBS solution containing 1:5,000 fluorescent microspheres (Tetraspeck, Invitrogen, USA). The coverslips were then mounted in a Ludin chamber (Life Imaging Services), where a buffer composed of an oxygen scavenger (glucose oxidase) and a reducing agent (2-mercaptoethylamine) was added (600 mL). The Ludin chamber was sealed with an 18-mm coverslip to prevent oxygen exchange.

Confocal imaging

Confocal imaging was captured with Leica SPE (63x oil immersion objective, N.A. 1.4). Excitation (λexc) and emission (λem) wavelengths were as follows: DAPI, Hoechst (λexc = 405 nm, λem = 430 – 480 nm), GFP (λexc = 488 nm, λem = 500 – 545 nm), mScarlet (λexc = 561 nm, λem = 570 – 610 nm) and Alexa Fluor-647 (λexc 635 nm, λem = 650 – 700 nm).

dSTORM imaging and reconstruction

dSTORM acquisitions in HEK293T cells were conducted on a homemade system built on a Nikon Eclipse Ti microscope, equipped with a 100x oil immersion objective (N.A. 1.49) (60). A 642 nm laser line was used to excite the Alexa Fluor-647 fluorophore, set to a power of 134 mW (resulting in an intensity of 2.7 kW/cm^2). Samples were imaged with an EM-CCD camera (Hamamatsu, ImagEM) maintained at -60°C. Z-stabilization was ensured by the Nikon Perfect Focus System integrated into the microscope. Acquisition was performed in TIRF mode controlled using Micro-Manager 1.4.23 (61). Single-molecule localization was achieved by analysis a stack of 15,000 images with the ThunderSTORM ImageJ plugin (62). The following parameters were used: image filtering – Difference-of-Gaussians filter (sigma 1 = 1.2 px, sigma 2 = 1.9 px), approximate localization of molecules: centroid of connected components (peak intensity threshold std (Wave.F1), sub-pixel localization of molecules: PSF: Integrated Gaussian (fitting radius: 6 px, fitting method: Weighted Least squares, initial sigma: 1.6 px)). Results were filtered by sigma, localization precision, and intensities values: 110 nm < sigma > 220 nm, precision < 25 nm and intensity < 2000.

dSTORM acquisitions in BV2 cells were performed on a commercial LEICA DMi8 (Leica, Germany) inverted microscope equipped with anti-vibrational table (TMC, USA) to minimize drift, along with a Leica HC PL APO 100X oil immersion TIRF objective (NA 1.47). For sample excitation, the microscope was equipped with a fiber-coupled laser launch composed of the following wavelengths: 405, 488, 532, 561, and 642 nm (Roper Scientific, Evry, France). Samples were imaged with an EMCCD camera (Teledyne Photometrics). Z stabilization was guaranteed by the Leica auto focus system integrated into the microscope. The 642 nm laser was used at a constant power to excite the Alexa Fluor-647 fluorophore, and the 405 nm laser was adjusted throughout the acquisition to control the level of single molecules per frame. Image acquisition was performed in TIRF mode controlled by MetaMorph software (Molecular Devices), with a 30 ms frame duration and a stack of 20,000 frames per acquisition on a 512 x 512-pixel ROI (pixel size = 160 nm).

Super-resolved images were reconstructed using the PALMTracer plugin for MetaMorph (63). The localizations were first extracted using a consistent intensity threshold across the entire dataset. Subsequently, super-resolved images were generated from these localizations with a pixel size of 40 nm. The density of localization was then extracted on each image, based on ROIs determined around the plasma membrane.

Cluster size measurement

Density-based clustering was performed using SR-Tesseler software (49) with the following input parameters: density factor 1 = 1; density factor 2 = 0.7, max length = 250 nm and min locs = 10; max locs = 200, max distance = 2 μm. The data obtained were further analyzed with GraphPad Prism (version 8.0.2).

Kinetic analysis of X7-uP labeling

The **X7-uP** labeling reaction follows a kinetic model in which a reversible ligand binding reaction (here **X7-uP**) precedes an irreversible chemical reaction, as described previously (41). In the presence of large excess of **X7-uP** relative to P2X7 sites, the pseudo-first-order reaction rate constant (k_{app}) is given by Eq. 1:

$$f(t) = \exp(-k_{app}t)$$

where t is the labeling reaction time at a given **X7-uP** concentration. The relationship between k_{app} and **X7-uP** concentration is described by Eq. 2:

$$k_{app} = \frac{k_L}{1 + K_d/[\text{X7-uP}]}$$

where K_d is the dissociation constant of **X7-uP** and k_L is the rate constant of the irreversible chemical reaction.

Data analysis

All experiments were conducted with at least three independent experiments. Statistical significance was assumed when the *P*-value was < 0.05. Graphs were generated using RStudio (version 1.4.1717) and ggplot2 package (version 3.3.5) or GraphPad prism.

For confocal data, membrane fluorescence intensities were manually selected using the ROI function of ImageJ (version 2.3.0/1.53f). Data were then analyzed using in-house written R scripts, employing the following packages: ggplot2, reshape2 (version 1.4.4), readxl (version 1.3.1), dplyr (version 1.0.7), Rmisc (version 1.5), and naniar (version .6.1).

For confocal data shown in Figure 5 — figure supplement 3, membrane intensities were automatically selected. A threshold was first applied to distinguish particles from the background, after which all particles >20 pixels in size were automatically selected and combined for each cell. After manually adjusting the selections, the integrated density (mean gray value x pixel number) was determined using ImageJ's Measure function. Data were then analyzed with GraphPad.

For cluster analysis, data extracted from SR-Tesseler (cluster diameter, number of detections per cluster, inter-cluster distance) were computed with GraphPad Prism for each cell.

Acknowledgments

We are grateful to Pr. P. Didier for training on dSTORM in HEK293T cells, Dr. F. Rassendren for providing P2X7-mScarlet and P2X-GFP constructs, and Pr. R. Schlichter for providing BV2 cells. This work was supported by the Agence Nationale de la Recherche (Grant ANR-20-CE14-0016-02), the Ministère de la Recherche (PhD grant to B.A., the International Center for Frontier Research in Chemistry (Labex CSC-TGR-18) (PhD grant to F.C.), The Région Grand Est (PhD grant to F.C.), the "École Universitaire de Recherche" Euridol (Programme d'investissement d'Avenir, ANR-17-EURE-0022) (PhD grant extension to B.A.) and was achieved within the NeuroStra Interdisciplinary Thematic Institute of the ITI 2021-2028 program of the University of

Strasbourg, CNRS and Inserm. This work has also benefitted from support provided by the University of Strasbourg Institute for Advanced Study (USIAS) for a fellowship, within the French national program “Investment for the future” (Idex-Unistra).

References

1. Burnstock G (2004) Introduction: P2 receptors. *Curr Top Med Chem* 4(8):793-803.
2. Jacobson KA*, et al.* (2020) Update of P2Y receptor pharmacology: IUPHAR Review 27. *Br J Pharmacol* 177(11):2413-2433.
3. Illes P*, et al.* (2021) Update of P2X receptor properties and their pharmacology: IUPHAR Review 30. *Br J Pharmacol* 178(3):489-514.
4. North RA (2002) Molecular physiology of P2X receptors. *Physiol Rev* 82(4):1013-1067.
5. Di Virgilio F, Dal Ben D, Sarti AC, Giuliani AL, Falzoni S (2017) The P2X7 Receptor in Infection and Inflammation. *Immunity* 47(1):15-31.
6. Ferrari D*, et al.* (1996) Mouse microglial cells express a plasma membrane pore gated by extracellular ATP. *J Immunol* 156(4):1531-1539.
7. Ferrari D*, et al.* (1997) Extracellular ATP triggers IL-1 beta release by activating the purinergic P2Z receptor of human macrophages. *J Immunol* 159(3):1451-1458.
8. Monif M, Burnstock G, Williams DA (2010) Microglia: proliferation and activation driven by the P2X7 receptor. *Int J Biochem Cell Biol* 42(11):1753-1756.
9. Bhattacharya A, Biber K (2016) The microglial ATP-gated ion channel P2X7 as a CNS drug target. *Glia* 64(10):1772-1787.
10. He Y, Taylor N, Fourgeaud L, Bhattacharya A (2017) The role of microglial P2X7: modulation of cell death and cytokine release. *J Neuroinflammation* 14(1):135.
11. Illes P (2020) P2X7 Receptors Amplify CNS Damage in Neurodegenerative Diseases. *Int J Mol Sci* 21(17).
12. Inoue K, Tsuda M (2021) Nociceptive signaling mediated by P2X3, P2X4 and P2X7 receptors. *Biochem Pharmacol* 187:114309.
13. Cao F*, et al.* (2019) P2X7 receptor: A potential therapeutic target for autoimmune diseases. *Autoimmun Rev* 18(8):767-777.
14. Kan LK, Williams D, Drummond K, O'Brien T, Monif M (2019) The role of microglia and P2X7 receptors in gliomas. *J Neuroimmunol* 332:138-146.
15. Douguet L*, et al.* (2021) A small-molecule P2RX7 activator promotes anti-tumor immune responses and sensitizes lung tumor to immunotherapy. *Nat Commun* 12(1):653.
16. Huang Z, Tan S (2021) P2X7 Receptor as a Potential Target for Major Depressive Disorder. *Curr Drug Targets* 22(10):1108-1120.
17. Huang S*, et al.* (2024) Disruption of the Na(+)/K(+)-ATPase-purinergic P2X7 receptor complex in microglia promotes stress-induced anxiety. *Immunity* 57(3):495-512 e411.
18. Martin E*, et al.* (2019) New role of P2X7 receptor in an Alzheimer's disease mouse model. *Mol Psychiatry* 24(1):108-125.
19. Volonte C, Apolloni S, Skaper SD, Burnstock G (2012) P2X7 receptors: channels, pores and more. *CNS Neurol Disord Drug Targets* 11(6):705-721.
20. Garcia-Marcos M*, et al.* (2006) Characterization and comparison of raft-like membranes isolated by two different methods from rat submandibular gland cells. *Biochim Biophys Acta* 1758(6):796-806.
21. Gonnord P*, et al.* (2009) Palmitoylation of the P2X7 receptor, an ATP-gated channel, controls its expression and association with lipid rafts. *FASEB J* 23(3):795-805.

22. Barth K*, et al.* (2008) Characterization of the molecular interaction between caveolin-1 and the P2X receptors 4 and 7 in E10 mouse lung alveolar epithelial cells. *Int J Biochem Cell Biol* 40(10):2230-2239.
23. Barth K*, et al.* (2007) Caveolin-1 influences P2X7 receptor expression and localization in mouse lung alveolar epithelial cells. *FEBS J* 274(12):3021-3033.
24. Garcia-Marcos M, Pochet S, Marino A, Dehaye JP (2006) P2X7 and phospholipid signalling: the search of the "missing link" in epithelial cells. *Cell Signal* 18(12):2098-2104.
25. Weinhold K, Krause-Buchholz U, Rodel G, Kasper M, Barth K (2010) Interaction and interrelation of P2X7 and P2X4 receptor complexes in mouse lung epithelial cells. *Cell Mol Life Sci* 67(15):2631-2642.
26. Raouf R, Chabot-Dore AJ, Ase AR, Blais D, Seguela P (2007) Differential regulation of microglial P2X4 and P2X7 ATP receptors following LPS-induced activation. *Neuropharmacology* 53(4):496-504.
27. Trang M, Schmalzing G, Muller CE, Markwardt F (2020) Dissection of P2X4 and P2X7 Receptor Current Components in BV-2 Microglia. *Int J Mol Sci* 21(22).
28. Janks L, Sharma CVR, Egan TM (2018) A central role for P2X7 receptors in human microglia. *J Neuroinflammation* 15(1):325.
29. Lord B*, et al.* (2015) A novel radioligand for the ATP-gated ion channel P2X7: [3H] JNJ-54232334. *Eur J Pharmacol* 765:551-559.
30. Choi HB, Ryu JK, Kim SU, McLarnon JG (2007) Modulation of the purinergic P2X7 receptor attenuates lipopolysaccharide-mediated microglial activation and neuronal damage in inflamed brain. *J Neurosci* 27(18):4957-4968.
31. Monif M, Reid CA, Powell KL, Smart ML, Williams DA (2009) The P2X7 receptor drives microglial activation and proliferation: a trophic role for P2X7R pore. *J Neurosci* 29(12):3781-3791.
32. Monif M*, et al.* (2016) Interleukin-1beta has trophic effects in microglia and its release is mediated by P2X7R pore. *J Neuroinflammation* 13(1):173.
33. Kaczmarek-Hajek K*, et al.* (2018) Re-evaluation of neuronal P2X7 expression using novel mouse models and a P2X7-specific nanobody. *Elife* 7.
34. Manz BN, Groves JT (2010) Spatial organization and signal transduction at intercellular junctions. *Nat Rev Mol Cell Biol* 11(5):342-352.
35. Choquet D, Sainlos M, Sibarita JB (2021) Advanced imaging and labelling methods to decipher brain cell organization and function. *Nat Rev Neurosci* 22(4):237-255.
36. Schermelleh L*, et al.* (2019) Super-resolution microscopy demystified. *Nat Cell Biol* 21(1):72-84.
37. Shrivastava AN, Rodriguez PC, Triller A, Renner M (2013) Dynamic micro-organization of P2X7 receptors revealed by PALM based single particle tracking. *Front Cell Neurosci* 7:232.
38. Gangadharan V, Nohe A, Caplan J, Czymmek K, Duncan RL (2015) Caveolin-1 regulates P2X7 receptor signaling in osteoblasts. *Am J Physiol Cell Physiol* 308(1):C41-50.
39. Kaczmarek-Hajek K, Lorinczi E, Hausmann R, Nicke A (2012) Molecular and functional properties of P2X receptors--recent progress and persisting challenges. *Purinergic Signal* 8(3):375-417.
40. Shiraiwa K, Cheng R, Nonaka H, Tamura T, Hamachi I (2020) Chemical Tools for Endogenous Protein Labeling and Profiling. *Cell Chem Biol* 27(8):970-985.

41. Tamura T*, et al.* (2018) Rapid labelling and covalent inhibition of intracellular native proteins using ligand-directed N-acyl-N-alkyl sulfonamide. *Nat Commun* 9(1):1870.
42. Karasawa A, Kawate T (2016) Structural basis for subtype-specific inhibition of the P2X7 receptor. *Elife* 5.
43. Guile SD*, et al.* (2009) Antagonists of the P2X(7) receptor. From lead identification to drug development. *J Med Chem* 52(10):3123-3141.
44. Michel AD*, et al.* (2007) Direct labelling of the human P2X7 receptor and identification of positive and negative cooperativity of binding. *Br J Pharmacol* 151(1):103-114.
45. Bhattacharya A*, et al.* (2013) Pharmacological characterization of a novel centrally permeable P2X7 receptor antagonist: JNJ-47965567. *Br J Pharmacol* 170(3):624-640.
46. Allsopp RC, Dayl S, Schmid R, Evans RJ (2017) Unique residues in the ATP gated human P2X7 receptor define a novel allosteric binding pocket for the selective antagonist AZ10606120. *Sci Rep* 7(1):725.
47. Surprenant A, Rassendren F, Kawashima E, North RA, Buell G (1996) The cytolytic P2Z receptor for extracellular ATP identified as a P2X receptor (P2X7). *Science* 272(5262):735-738.
48. Karasawa A, Kawate T (2017) Expression and Purification of a Mammalian P2X7 Receptor from Sf9 Insect Cells. *Bio Protoc* 7(17).
49. Levet F*, et al.* (2015) SR-Tesseler: a method to segment and quantify localization-based super-resolution microscopy data. *Nat Methods* 12(11):1065-1071.
50. Perregaux DG, McNiff P, Laliberte R, Conklyn M, Gabel CA (2000) ATP acts as an agonist to promote stimulus-induced secretion of IL-1 beta and IL-18 in human blood. *J Immunol* 165(8):4615-4623.
51. Ferrari D*, et al.* (2006) The P2X7 receptor: a key player in IL-1 processing and release. *J Immunol* 176(7):3877-3883.
52. Swanson KV, Deng M, Ting JP (2019) The NLRP3 inflammasome: molecular activation and regulation to therapeutics. *Nat Rev Immunol* 19(8):477-489.
53. Dunning K*, et al.* (2021) P2X7 Receptors and TMEM16 Channels Are Functionally Coupled with Implications for Macropore Formation and Current Facilitation. *Int J Mol Sci* 22(12).
54. Franceschini A*, et al.* (2015) The P2X7 receptor directly interacts with the NLRP3 inflammasome scaffold protein. *FASEB J* 29(6):2450-2461.
55. Miras-Portugal MT, Sebastian-Serrano A, de Diego Garcia L, Diaz-Hernandez M (2017) Neuronal P2X7 Receptor: Involvement in Neuronal Physiology and Pathology. *J Neurosci* 37(30):7063-7072.
56. Illes P, Khan TM, Rubini P (2017) Neuronal P2X7 Receptors Revisited: Do They Really Exist? *J Neurosci* 37(30):7049-7062.
57. Bindels DS*, et al.* (2017) mScarlet: a bright monomeric red fluorescent protein for cellular imaging. *Nat Methods* 14(1):53-56.
58. Habermacher C*, et al.* (2016) Photo-switchable tweezers illuminate pore-opening motions of an ATP-gated P2X ion channel. *Elife* 5:e11050.
59. Olivier N, Keller D, Rajan VS, Gonczy P, Manley S (2013) Simple buffers for 3D STORM microscopy. *Biomed Opt Express* 4(6):885-899.
60. Glushonkov O, Real E, Boutant E, Mely Y, Didier P (2018) Optimized protocol for combined PALM-dSTORM imaging. *Sci Rep* 8(1):8749.

966 61. Edelstein AD*, et al.* (2014) Advanced methods of microscope control using muManager
967 software. *J Biol Methods* 1(2).
968 62. Ovesny M, Krizek P, Borkovec J, Svindrych Z, Hagen GM (2014) ThunderSTORM: a
969 comprehensive ImageJ plug-in for PALM and STORM data analysis and super-resolution
970 imaging. *Bioinformatics* 30(16):2389-2390.
971 63. Butler C*, et al.* (2022) Multi-Dimensional Spectral Single Molecule Localization
972 Microscopy. *Front Bioinform* 2:813494.

973
974

Figures

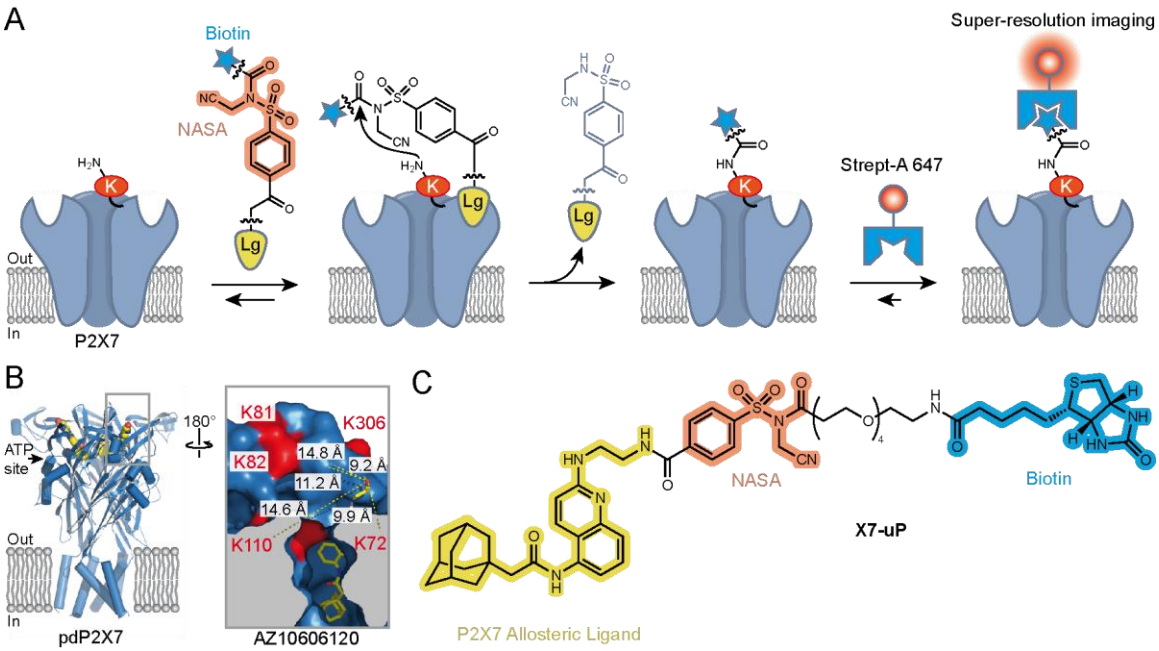

Figure 1. Affinity-guided labeling strategy for P2X7. (**A**) Schematic representation of the P2X7 labeling strategy using ligand-directed *N*-cyanomethyl NASA chemistry. The biotin tag on the NASA molecule enables super-resolution imaging of nanoscale P2X7 localization using Strept-A 647 probe through a highly specific biotinylation reaction involving endogenous lysine (K) residues. Lg: P2X7 ligand. (**B**) Crystal structure of panda P2X7 (pdP2X7) shown in ribbon representation, bound to AZ10606120 depicted as spheres (PDB:5U1W) (42, 48). One of the three ATP-binding sites and the approximate location of the membrane are also indicated. Inset, enlarged view of the AZ10606120-binding pocket, rotated 180°. Distances (in Å) between the α-carbon of selected lysines and the hydroxyl group of AZ10606120 are displayed. Note that K300 is not visible in this view. (**C**) Chemical structure of **X7-uP**.

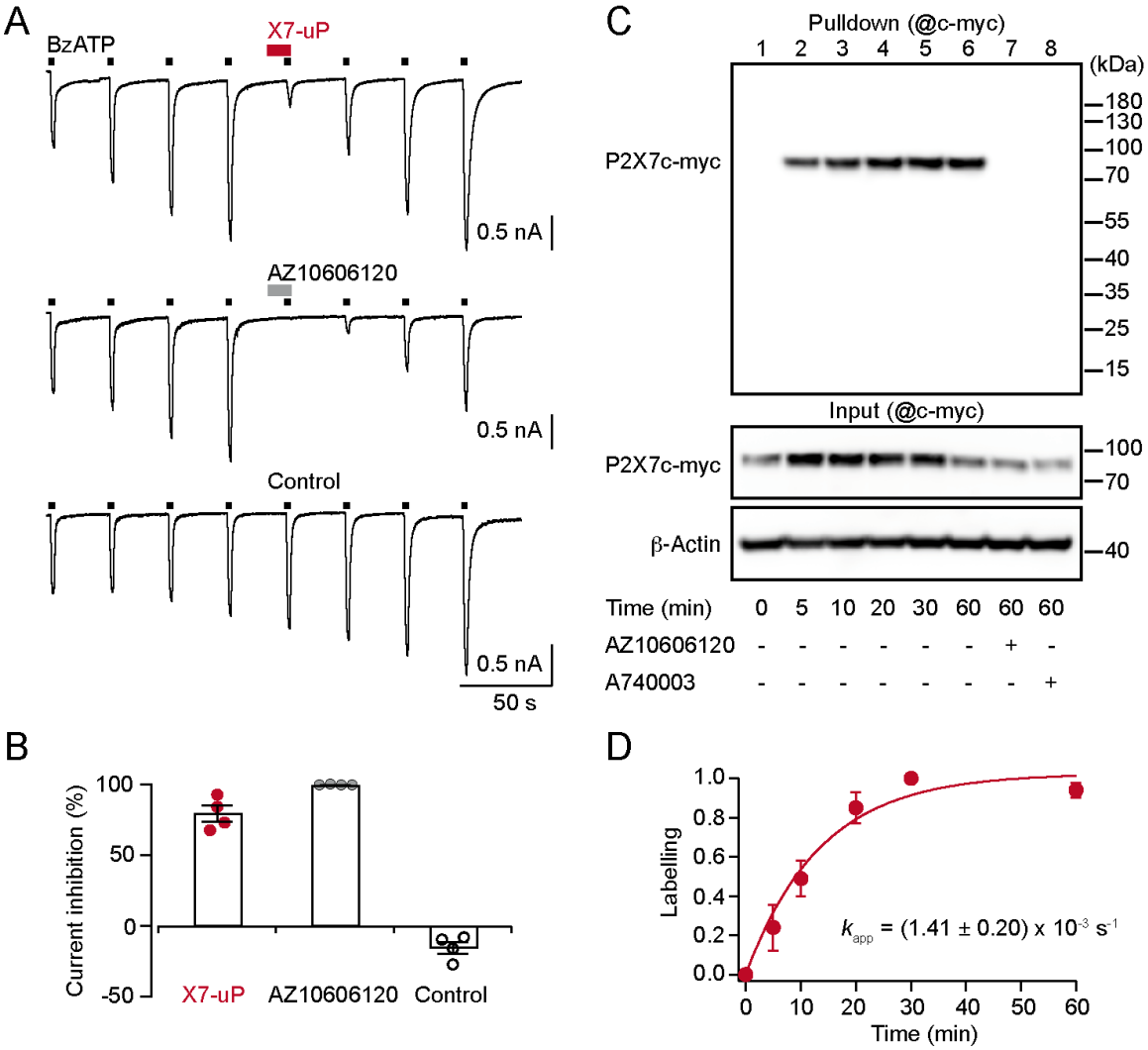

Figure 2. X7-uP is a potent P2X7 inhibitor that rapidly labels ectopically expressed P2X7 in HEK293T cells. (**A**) Whole-cell currents evoked by 10 μM BzATP are reversibly inhibited by co-applying 1 μM **X7-uP** (upper trace) or 1 μM AZ10606120 (middle trace) in cells transiently transfected with rP2X7. Inhibitors were pre-applied alone for 8 s before 2 seconds of co-application. In the control (absence of inhibitors), BzATP-induced currents further increased, demonstrating current facilitation, which is an expected feature of P2X7 activation (47). (**B**) Summary of whole-cell inhibition (n = 4 cells for each condition). Bars represent mean ± s.e.m. (**C**) Western blot analysis of P2X7 labeling by **X7-uP**. Cells transiently transfected with P2X7c-myc were treated with 1 μM **X7-uP** for 0-60 minutes, in the absence or presence of 10 μM AZ10606120 or 10 μM A740003 (as indicated), followed by extensive washing. After cell lysis, biotinylated proteins were pulled down, separated on SDS-PAGE, and Western blotting was revealed using an anti-c-myc antibody (@c-myc). Molecular mass markers are shown on the right. Control of P2X7c-myc expression is presented in the corresponding input. β-Actin was used as a loading control. (**D**) Time course plot of P2X7 labeling with 1 μM **X7-uP**. Data (mean ± s.e.m., n = 3 independent transfections) were fitted with Eq. (1) to determine the pseudo-first-order reaction rate k_{app} (mean ± s.e.m.).

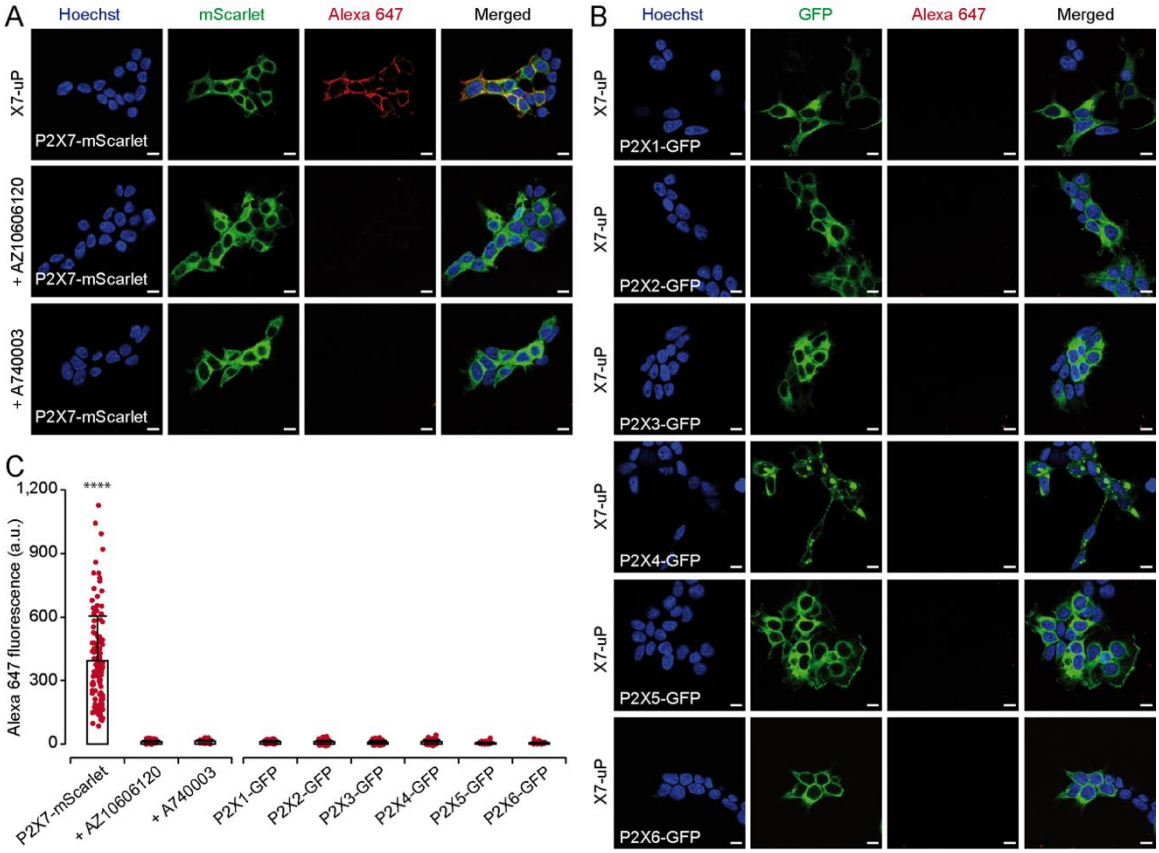

Figure 3. X7-uP labeling is highly selective for P2X7. (**A-B**) Confocal images of HEK293T cells transiently transfected with either P2X7-mScarlet (**A**) or various P2X subunits tagged with GFP (P2X1-GFP, P2X2-GFP, P2X3-GFP, P2X4-GFP, P2X5-GFP, or P2X6-GFP) (**B**) were labeled with **X7-uP** and revealed using Strept-A 647 (red) in FBS-free DMEM. Labeling was performed in the presence of 10 μM AZ10606120 or 10 μM A740003 (**A**). Nuclei were stained with Hoechst (blue). For clarity, mScarlet and GFP signals are displayed in green. Scale bars, 10 μm. (**C**) Quantification of Alexa 647 fluorescence. Bars represent mean ± standard deviation (s.d.) (n = 75-129 cells, *t*-test comparisons to P2X7-mScarlet, ****$P < 0.0001$.

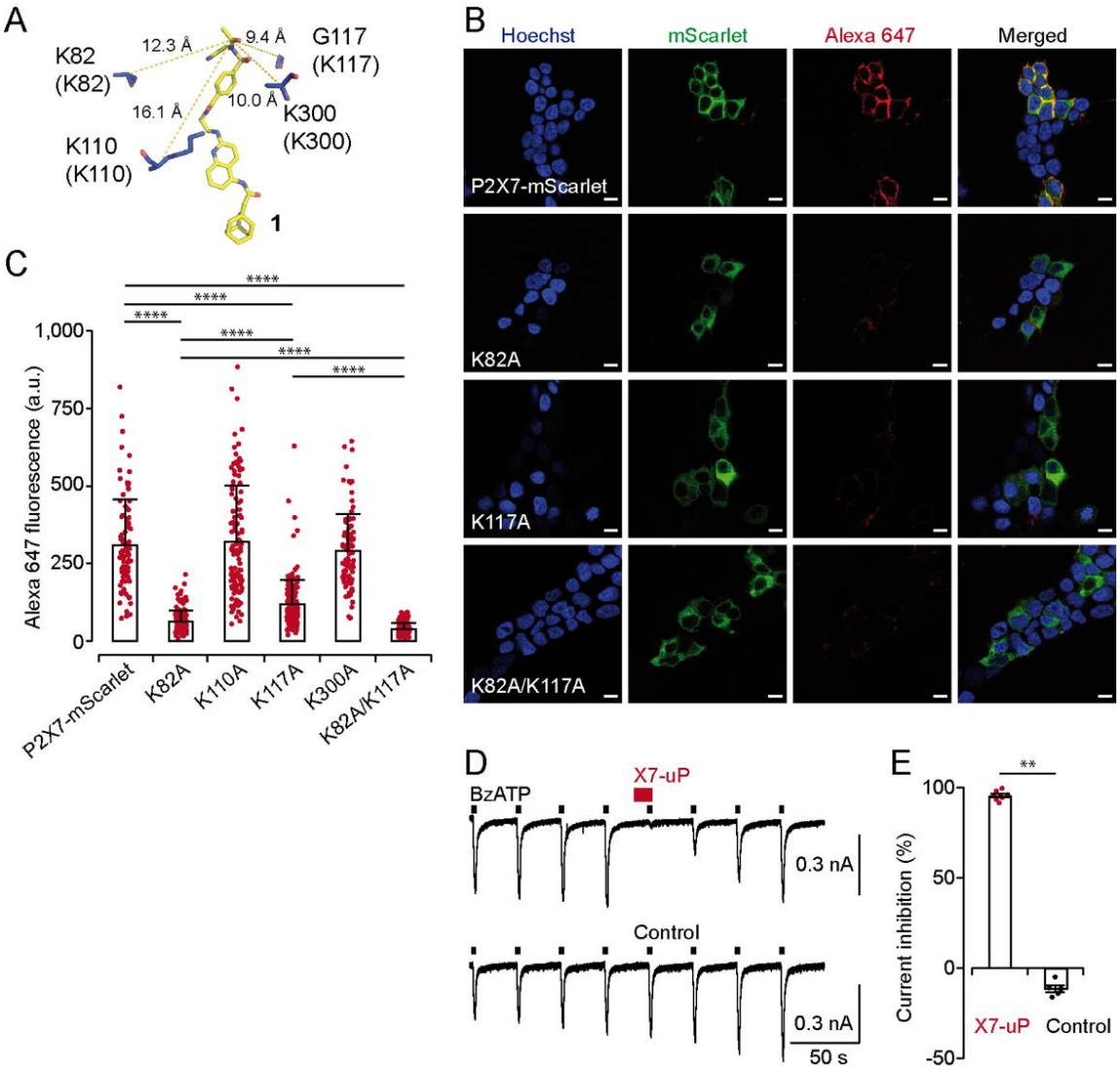

Figure 4. X7-uP labels K82 and K117 in rat P2X7. (**A**) Molecular docking of **1** (same pose as shown in Figure 1 — figure supplement 1C) in pdP2X7, showing distances (in Å) between the reactive carbonyl of **1** (stick representation) and selected α-carbons of nearby residues (blue). Residues shown in parentheses correspond to equivalent rP2X7 residues. (**B**) Confocal images of HEK293T cells transiently transfected with different P2X7 constructs: P2X7-mScarlet, K82A, K117A, and K82A/K117A. Scale bars, 10 μm. (**C**) Quantification of Alexa 647 fluorescence. Bars represent mean ± s.d. (n = 90-190 cells, *t*-test comparisons to indicated conditions, ****$P < 0.0001$). (**D**) Whole-cell currents evoked by 10 μM BzATP are reversibly inhibited by co-application of 0.5 μM **X7-uP** (upper trace) to BzATP in a cell transiently transfected with the double mutant K82A/K117A. The control (absence of **X7-uP**) is shown in the bottom trace. (**E**) Summary of whole-cell inhibition for K82A/K117A (n = 7 cells for **X7-uP** and 5 cells for control). Bars represent mean ± s.e.m.; Mann-Whitney test (**$P < 0.005$).

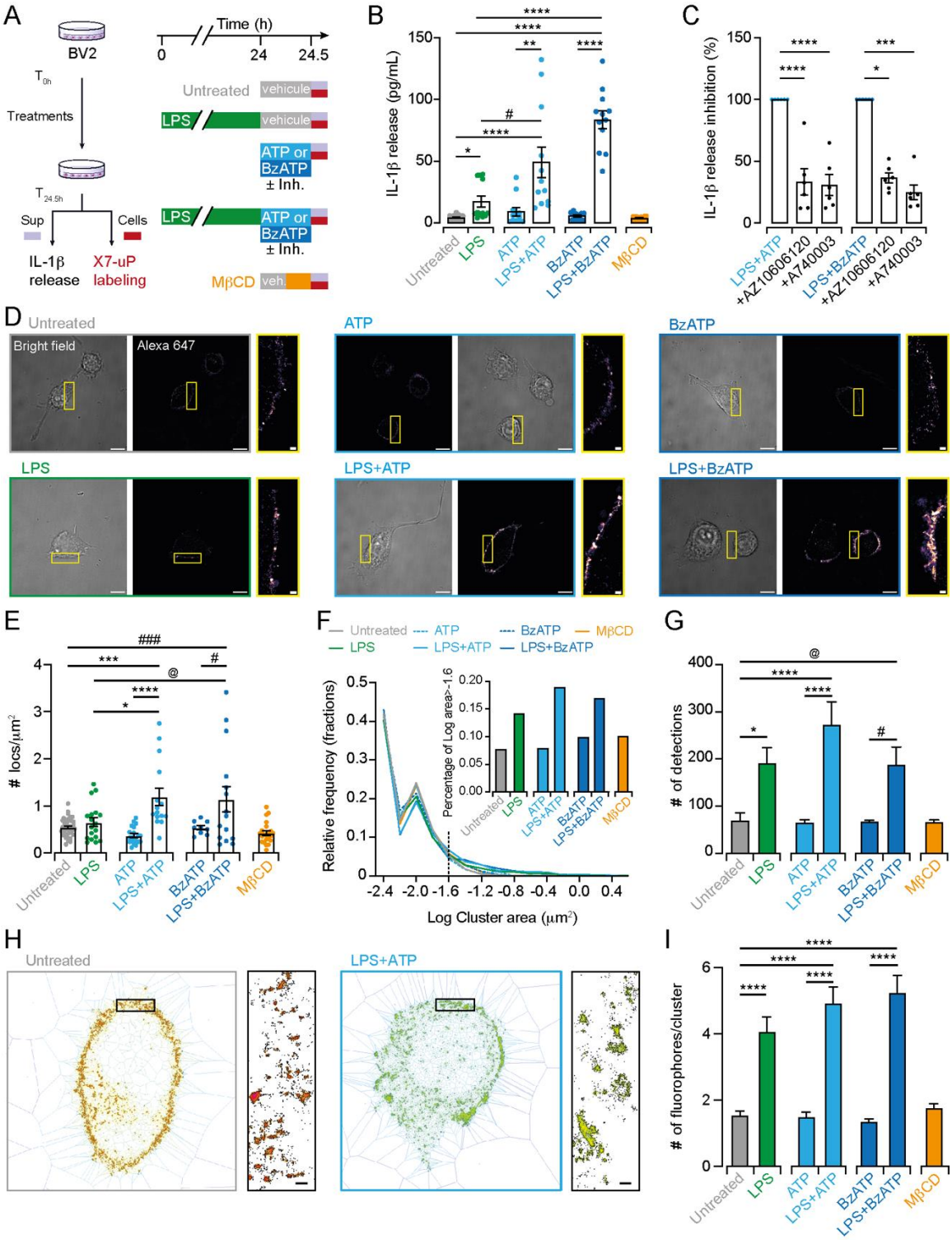

Figure 5. dSTORM data revealed nanoscale P2X7 plasma membrane localization in BV2 cells. (**A**) Cartoon and experimental timeline of BV2 cell treatments. IL-1β release was assessed in the supernatant (sup), and the same cells were labeled with 1 mM **X7-uP** after extensive washout. (**B**) Quantification of IL-1β release by ELISA following the indicated treatments: LPS (1 mg/mL for 24 h), ATP (1 mM for 30 min), BzATP (300 mM for 30 min), and MβCD (15 mM for 15

min). Bars represent mean ± s.e.m. (n = 12 samples from 3 independent experiments). Data were compared using Kruskal-Wallis followed by Dunn's multiple comparisons (**P* = 0.0208, #*P* = 0.0362, ***P* = 0.0014, *****P* < 0.0001). (**C**) Normalized quantification of IL-1β release induced by LPS+ATP or LPS+BzATP in the presence of P2X7 inhibitors AZ10606120 or A740003. Bars represent mean ± s.e.m. (n = 6 samples from 6 independent experiments). One-way ANOVA with Dunnett's multiple comparisons to control condition for ATP data (*****P* < 0.0001). Kruskal-Wallis followed by Dunn's multiple comparisons to control condition for BzATP data (**P* = 0.0414, *** *P* = 0.0006). (**D**) Bright-field and dSTORM images of **X7-uP**-labeled BV2 cells revealed with Strept-A 647 corresponding to experiments shown in panel b. Scale bars, 10 mm. Insets: Magnified dSTORM images. Scale bars, 1 mm. (**E**) Quantification of single P2X7 localization density. Bars represent mean ± s.e.m. (each data point represent a cell, n = 3 independent experiments). One-way ANOVA with Tukey's multiple comparisons (**P* < 0.019, #*P* < 0.0194, @*P* < 0.0477, ****P* < 0.0002, ###*P* < 0.0008, *****P* < 0.0001). (**F**) Relative frequency of cluster size. Inset: percentage of clusters larger than 0.025 mm^2. (**G**) Number of detections per cluster. Bars represent mean ± s.e.m. One-way ANOVA with Tukey's multiple comparisons (**P* < 0.0197, #*P* < 0.0277, @*P* < 0.0389, *****P* < 0.0001). (**H**) Images showing tessellation analysis of cells treated either with LPS+ATP or left untreated. Inset: magnification. Scale bars, 200 nm. (**I**) Number of fluorophores per cluster. Bars represent mean ± s.e.m. One-way ANOVA with Tukey's multiple comparisons (*****P* < 0.0001).

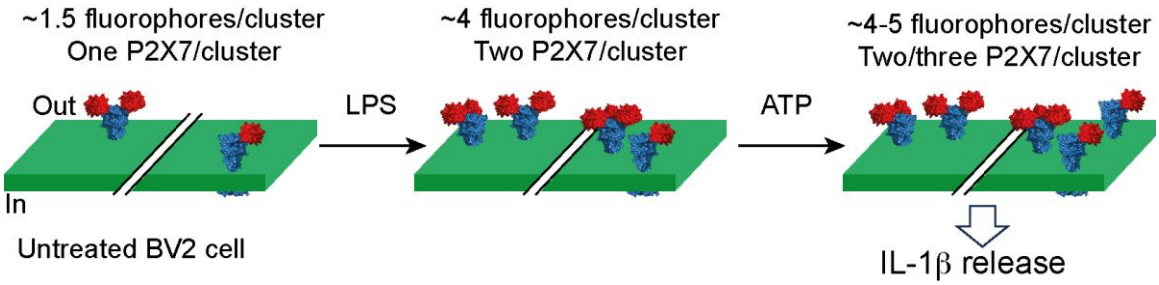

Figure 6. Nanoscale redistribution of individual P2X7 receptors in microglia under pro-inflammatory conditions at the plasma membrane. The cartoon illustrates two distinct clusters of P2X7 receptors (blue), each adorned with one, two, or three fluorescently tagged tetrameric biotin-bound streptavidin (red). In untreated cells, each cluster contains an average of 1.5 fluorophores per P2X7 receptor. Treatment with LPS and ATP promotes P2X7 clustering by increasing the average number of fluorophores per cluster to between 4 and 5, resulting in an increased number of P2X7 receptors per cluster, from one to three. This redistribution synergistically triggers IL-1β release.